**THE UNIVERSITY OF MICHIGAN,**
**DEPARTMENT OF ATMOSPHERIC, OCEANIC AND SPACE SCIENCE,**

**Space Physics Research Laboratory,**
**2455 Hayward St.,**
**Ann Arbor, Michigan 48109-2143.**

| | |
|---|---|
| **Contract/Grant No.:** | NAGW 3457 |
| **Project Name:** | Data analysis and theoretical studies of the upper mesosphere and lower thermosphere |
| **Report Author(s):** | Alan Burns |
| **Author(s) Phone:** | (313)-763-6246 |
| **Preparation Date:** | February 4, 1994 |
| **Report Type:** | Annual Report |
| **Period Covered:** | April 1993 - April 1994 |
| **Project Director:** | T. L. Killeen |
| **Principal Investigator(s):** | T. L. Killeen |
| **Program Technical Officer/Address:** | Dr. M. Mellott,<br>Code ES,<br>NASA Headquarters,<br>Washington, DC, 20546. |

# DATA ANALYSIS AND THEORETICAL STUDIES OF THE UPPER MESOSPHERE AND LOWER THERMOSPHERE

## 1). Summary.

The work proposed under this grant came in three parts. The first involved extending our continuing study of electrodynamical feedback between the thermosphere/ionosphere and the magnetosphere. The second was a model-experiment comparison study of global dynamics and the third was a "spectral energetics" analysis of tidal dissipation and energy exchange mechanisms.

In the past year progress has been made on all three topics. A paper is in press about electrodynamic feedback, and another is also in press on an element of the "spectral energetics" analysis. Furthermore, a paper is being prepared an global dynamics variations in response to geomagnetic storms. In addition, much of the data needed for further studies on global dynamics is being prepared for inclusion in a relational database.

This report is organized into several separate sections. In the next section we present an introduction to the work that we are doing in this proposal. We discuss the progress made in our work and some results in section 3. In the last section, we sum up this work.

## 2). Introduction

The Earth's mesosphere and lower-thermosphere/ionosphere (MLTI), between ~60 and 180 km altitude, is the most poorly understood region of the Earth's atmosphere, primarily because of its relative inaccessibility. This lack of knowledge has been widely recognized and has provided important scientific rationale for the upcoming NASA TIMED mission [*Killeen et al.*, TIMED Science Definition Team, Volume II, 1991]. While the data gathered during the TIMED era will revolutionize our understanding of the MLTI règion, much work can be done prior to the mission, both to develop data-analysis and modeling techniques and to study the more limited relevant experimental data from previous missions. The grant reported on here continues and extends an existing successful program of scientific research into the energetics, dynamics and electrodynamics of the MLTI, using available theoretical and data analysis tools.

Our previous work under this grant (NAGW-1535) focused on two areas. The first was a theoretical study of the bi-directional coupling between the MLTI and the

magnetosphere [*Deng et al.*, 1991; 1993]. We have used the NCAR thermosphere-ionosphere general circulation model (TIGCM) to calculate the time-dependent magnitudes of the Hall and field-aligned currents that occur in the recovery phase of geomagnetic storms, driven by the inertia of the neutral gas - the so-called "flywheel effect" [*Lyons et al.*, 1985]. Such currents flow in opposite directions to those more typically associated with the direct magnetospherically-driven system and correspond to electrical energy flowing upwards from the ionosphere. For the first time, our work experimentally demonstrated the existence of a small but significant flywheel effect through comparisons of theoretical calculations and data from DE-2 [*Deng et al.*, 1991; 1993].

Under the grant reported upon here, we proposed a three-year effort to supplement and extend this previous work, focusing on scientific areas of direct relevance to TIMED objectives. Three overlapping studies were proposed, the first two represented extensions of current efforts and the third represented a brand new approach to the study of MLTI energetics. The studies were:

1. An extension of our ongoing theoretical study of the electrodynamical feedback (flywheel) mechanism between the MLTI and the magnetosphere, using specialized post-processors developed by us for use with the NCAR TIEGCM (an updated version of the TIGCM);
2. An experimental study of the global dynamics of the lower thermosphere, using our recently developed wind inversion technique to interpret data from the Fabry-Perot Interferometer (FPI) on Dynamics Explorer-2 (DE-2);
3. A "spectral energetics" analysis of tidal dissipation and energy exchange mechanisms in the MLTI region, using spectral post-processors recently developed for use with the NCAR TIEGCM.

## 3). Progress in the Last Year.

The major thrust of our work in the past year has involved the first two tasks that were proposed under this grant. In the first of these, we have been working towards gaining a greater understanding of the electrodynamic feedback processes, wherein changes in the neutral thermosphere can affect the way magnetospheric energy is dissipated, and can even lead to times when the neutral thermospheric motion can drive a high latitude current system that is dissipated in the magnetosphere. To this end our work in the last year has been directed primarily towards developing a better one-dimensional, hybrid satellite track

model to study the effects of the dissipation of magnetospheric currents in the thermosphere and the way that these can affect the thermal/dynamic regime in the thermosphere.

This model is based on the *Emery et al.* (1985) satellite track code, but it also includes elements of the *Roble et al.* (1987) global mean thermosphere/ionosphere model and subsequent developments of the Roble et al. code. The earlier version of this satellite track model was described by *Emery et al.* (1985). The current version uses DE 2 (Dynamics Explorer 2) measurements of energetic electron spectra in an auroral code to determine particle ionization rates. A solar flux model is used to give the ionization, dissociation and heating caused by light in the EUV and UV regions of the spectrum. In addition, the electron densities and ion drifts measured by the DE 2 satellite are used as an upper boundary condition for the model. Ionospheric processes below the satellite orbit are modeled theoretically using the *Roble et al.* (1987) mean thermosphere/ionosphere code. Background neutral composition and temperatures are specified using MSIS-90 (*Hedin et al.*, 1991), while neutral winds are calculated using a modified version of the *Killeen et al.* (1987) VSH model.

In the paper that is soon to be published we used this model to study electron densities, ionization rates, particle heating rates, Hall and Pedersen conductivities and the dissipation of magnetospheric currents in the form of Joule heating. In addition, we performed model-data comparisons between a model run made for conditions appropriate to an overflight of the Chatanika radar facility. The principal results of this study are included in the conclusions of the attached paper (*Deng et al.*, 1994). Briefly summarized these are: there is a good first order agreement between DE 2 calculated Poynting fluxes and the height integrated energy conversion rate in the one-dimensional model; generally the dissipation of ionospheric currents is dominated by Joule heating, however over the polar cap the conversion of this electric energy into neutral wind mechanical energy is significant; and the model can reproduce the experimentally determined conductivites and Joule heating rates with reasonable fidelity, but it cannot reproduce all of the details of the radar measurements that were made in the auroral oval.

The work outlined above formed a substantial portion of Mr. Wei Deng's Ph. D. thesis. He successfully defended his thesis in November 1993. Work will continue on these studies in the next two years.

We have also done substantial work on general circulation. A paper is being prepared for submission that will describe changes in circulation in the upper thermosphere that occur as a result of geomagnetic storms. This work will act as a lead in to further work on circulation changes in the lower thermosphere that are driven by geomagnetic storms.

Over the next two years we plan to categorize the general meridional circulation of the region between 100 and 200 km with the 5577 Å "green line" data that are available. To this end, in the past year we have developed and processed data files for each orbit during which these data were available. We now have wind data from all of the 228 orbits that could be processed. While this in no way constitutes comprehensive coverage, it does provide some insight into the circulation in a number of differing sets of geophysical conditions. In particular, there are a surprising amount of data available for times when geomagnetic storms exist. This will enable us to perform the first global study of the way meridional neutral winds change in response to geomagnetic storms in the region between 100 and 150 km - the region of transition from the storm-driven regime to that not strongly affected by geomagnetic storms. At present we are developing a data base system that will make intercomparisons of these "green line" data simple, thus increasing our knowledge of the relationships between the wind data and geophysical inputs.

An initial paper reporting on our "spectral energetics" analysis of tidal dissipation and energy dissipation in the MLTI region is in press in the proceedings of the Chapman conference in Asilomar, CA. In this paper the concept of available potential energy was used with spectral decomposition to gain a greater understanding of the dissipation of tidal modes in the lower thermosphere. Our main conclusions were that: in contrast to the lower atmosphere, kinetic energy exceeds the available potential energy; the upwardly propagating diurnal and semi-diurnal tides carry most of the kinetic energy component; and the total potential energy is three orders of magnitude larger than either the available potential energy or the kinetic energy.

## 4). Concluding Remarks

Overall this has been a successful year. We have made progress in each of the three main topics proposed. Two papers are in press and two are in preparation on various topics related to this grant. In addition, a presentation related to the first topic will be made at the forthcoming COSPAR meeting in Hamburg, Germany. As well as these visible signs of progress, we have also progressed in the background work necessary for the continuing success of this grant. In particular, the development of a relational database comprising both the "green line" winds and relevant geophysical data is rapidly reaching a mature state. These studies will continue through the next year of the grant, during which time we hope that the progress in this work is as great as it has been in the last 12 months.

## 5). References


Deng, W., T. L. Killeen, A. G. Burns and R. G. Roble, The Flywheel Effect: Ionospheric Currents After a Geomagnetic Storm, Geophys. Res. Lett., 18, 1845-1849, 1991.

Deng, W., T. L. Killeen, A. G. Burns, R. G. Roble, J. Slavin and L. E. Wharton, The effects of neutral inertia on ionospheric currents in the high latitude thermosphere following a geomagnetic storm, J. Geophys. Res., 98, 7775-7790, 1993.

Deng, W., T. L. Killeen, A. G. Burns, R. M. Johnson, B. A. Emery, R. G. Roble, J. D. Winningham and J. B. Gary, A one-dimensional hybrid satellite track model for the Dynamics Explorer-2 (DE-2) satellite, *in press,* J. Geophys. Res., 1994.

Emery, B. A., R. G. Roble, E. C. Ridley, T. L. Killeen, M. H. Rees, J. D. Winningham, G. R. Carignan, P. B. Hays, R. A. Heelis, W. B. Hanson, N. W. Spencer, L. H. Brace, and M. Sugiura, Thermospheric and ionospheric structure of the Southern Hemisphere polar cap on 21 October 1981 as determined by Dynamics Explorer-2 satellite data, J. Geophys. Res., 90, 6553-6566, 1985.

Hedin, A. E., M. A. Biondi, R. G. Burnside, G. Hernandez, R. M. Johnson, T. L. Killeen, C. Mazaudier, J. W. Meriwether, J. E. Salah, R. J. Sica, R. W. Smith, N. W. Spencer, V. B. Wickwar and T. S. Virdi, Revised global model of thermosphere winds using satellite and ground based observations, J. Geophys. Res., 96, 7657-7688, 1991.

Killeen, T. L., R. G. Roble and N. W. Spencer, A computer model of global thermospheric wind and temperatures, Adv. Space Res., 7, 207-215, 1987

Lyons, L. R., T. L. Killeen, and R. L. Walterscheid, The neutral wind "flywheel" as a source of quiet-time, polar cap currents, Geophys. Res. Lett., 12, 101, 1985.

Roble, R. G., E. C. Ridley and R. E. Dickinson, On the global mean structure of the thermosphere, J. Geophys. Res., 92, 8745-8758, 1987.

# A One-Dimensional Hybrid Satellite Track Model for the Dynamics Explorer-2 (DE-2) Satellite

**W. Deng, T. L. Killeen, A. G. Burns and R. M. Johnson**
Space Physics Research Laboratory
Department of Atmospheric, Oceanic and Space Sciences
The University of Michigan, Ann Arbor, MI 48109-2143

**B. A. Emery and R. G. Roble**
National Center for Atmospheric Research, Boulder, CO 80307

**J. D. Winningham**
Department of Space Sciences
Southwest Research Institute, San Antonio, TX 78284

**J. B. Gary**
University of Texas at Dallas, Richardson, TX 75083

Submitted
~~For submission~~ to the Journal of Geophysical Research

September 24, 1993

Abstract

A one-dimensional hybrid satellite track model has been developed to calculate the high-latitude thermospheric/ionospheric structure below the satellite altitude using Dynamics Explorer-2 (DE-2) satellite measurements and theory. This model is based on the *Emery et al.* [1985] satellite track code, but also includes elements of the *Roble et al.* [1987] global mean thermosphere/ionosphere model. A number of parameterizations and data handling techniques are used to input satellite data from several DE-2 instruments into this model. Profiles of neutral atmospheric densities are determined from the MSIS-90 model and measured neutral temperatures. Measured electron precipitation spectra are used in an auroral model to calculate particle impact ionization rates below the satellite. These rates are combined with a solar ionization rate profile and used to solve the $O^+$ diffusion equation, with the measured electron density as an upper boundary condition. The calculated $O^+$ density distribution, as well as the ionization profiles, are then used in a photochemical equilibrium model to calculate the electron and molecular ion densities. The electron temperature is also calculated by solving the electron energy equation with an upper boundary condition determined by the DE-2 measurement. The model enables calculations of altitude profiles of conductivity and Joule heating rate along and below the satellite track. In a first application of the new model, a study is made of thermospheric and ionospheric structure below the DE-2 satellite for a single orbit which occurred on 25 October 1981. The field-aligned Poynting flux, which is independently obtained for this orbit, is compared with the model predictions of the height-integrated energy conversion rate. Good quantitative agreement between these two estimates has been reached. In addition, measurements taken at the Incoherent Scatter Radar site at Chatanika (65.1°N, 147.4°W) during a DE-2 overflight are compared with the model calculations. The results of this comparison indicate that the updated satellite track model provides reasonably accurate calculations of lower thermospheric conductivity and Joule heating rates.

# 1. Introduction

Comprehensively instrumented satellites have been used to study high-latitude thermosphere and ionosphere processes for a number of years. The Dynamics Explorer 2 (DE-2) satellite, in particular, was instrumented to measure auroral particles and fields, as well as neutral atmospheric and ionospheric parameters within the high-latitude thermosphere. These measurements have greatly improved our understanding of the various physical processes in this region. However, a significant gap in knowledge and understanding still exists in the lower thermosphere/ionosphere due to relative inaccessibility of this region to direct experimental approaches. Several detailed numerical models have been developed to study the dynamics and energetics of the thermosphere and ionosphere, including the lower thermospheric region. In particular, the National Center for Atmospheric Research Thermosphere-Ionosphere General Circulation Model (NCAR-TIGCM) has had a large measure of success in calculating wind and temperature fields similar to those observed from the DE-2 satellite [*Hays et al.*, 1984; *Roble et al.*, 1984; *Killeen et al.*, 1986; *Killeen and Roble*, 1988]. A one-dimensional global mean thermosphere/ionosphere/mesosphere model has also been developed to study the global average structure in this region within the framework of NCAR-TIGCM [*Roble et al.*, 1987; *Roble and Dickinson*, 1989]. The calculated global average structure from this model compares well with the globally averaged structure determined from ionospheric and thermospheric empirical models.

Large scale numerical models such as the NCAR-TIGCM require the parameterization of auroral energy and momentum inputs to the neutral thermosphere. The AMIE technique of *Richmond and Kamide* [1988] uses a data assimilation method to provide such inputs and is critically dependent on knowledge of the ionospheric conductivities in the lower thermospheric dynamo region. The study of energy exchange between the magnetosphere and ionosphere also requires detailed information on Joule heating rates in the lower thermosphere. It is therefore of value to develop a "satellite track" model that uses direct satellite measurements in the upper thermosphere to estimate the conductivity and Joule heating rates in the lower thermosphere.

Several satellite-based empirical models have been constructed to describe electric conductivities [*Wallis and Budzinski*, 1981; *Fuller-Rowell and Evans*, 1987], electric fields [*Heppner*, 1977; *Heelis* et al., 1982; *Foster et al.*, 1983a] and Joule heating [*Foster et al.*, 1983b; *Heelis and Coley* 1988]. *Emery et al.* [1985] developed a satellite track model that uses the DE-2 measurements to calculate the ionospheric/thermospheric structure down to about 80 km below the satellite orbit. This model has also been used to study the Joule heating rate in the lower thermosphere and mesosphere for a proton auroral event [*Roble et al.*, 1989], but these model predictions have not been compared with direct experimental data from the lower

thermosphere. In this paper, we extend the work of Emery et al. to include the ionospheric processes that are modeled in the global mean thermosphere/ionosphere model. We also compare the extended satellite track model predictions with measurements taken at the Incoherent Scatter Radar site at Chatanika (65.1°N, 147.4°W) during a DE-2 overflight. The extended model is then used to study the ionospheric structures below a single satellite orbit from October 25, 1981. Finally, we compare the model predictions of the height-integrated energy conversion rate with the field-aligned Poynting flux, which is independently calculated for this orbit [*Gary et al.*, 1993]. Our study shows that the extended satellite track model allows for high-latitude conductivities and Joule heating rates to be determined in the lower thermosphere with a reasonable accuracy, using *in situ* measurements along the satellite track. It can also provide a near "instantaneous picture" of the ionospheric structure below the satellite orbit.

## 2. Model

The earlier version of the satellite track model was described in detail by *Emery et al.* [1985]. Briefly, it uses DE-2 measurements of energetic electron spectra in an auroral code to determine the particle ionization rates. The measured ion drifts and electron densities, as well as a model of solar flux, are also used as model inputs. The electron and ion densities, temperatures, conductivities and Joule heating rates, as well as particle and solar heating rates, are calculated from these inputs in a neutral atmosphere modified to reproduce the measured temperature and $O/N_2$ ratio at the satellite altitude.

We have extended the Emery et al. satellite track code using a hybrid approach. In this scheme, we utilize the global mean thermosphere/ionosphere code of *Roble et al.*, [1987] to model the ionospheric processes below the satellite orbit theoretically. The empirical and semi-empirical MSIS-90 and VSH [*Killeen et al.* 1987] models are used to determine the neutral atmosphere structure and winds. A parameterized version of the solar EUV and UV flux measured from the Atmosphere Explorer satellites is also used to calculate photoionization rates of the major ion species. The auroral ionization rates are calculated following the method of Rees [1963, 1969] and Rees et al. [1971]. The electron flux needed in this calculation is determined from the LAPI measurements. The one-dimensional $O^+$ diffusion equation derived by *Roble et al.* [1987] is then solved in a constant pressure surface coordinate system using the calculated photoionization rates and the auroral ionization rates. The vertical coordinate system consists of 13 pressure levels ranging from approximately 97 km to 600 km. The use of a pressure coordinate system ensures that the normalized auroral ionization rates determined from the DE-2 electron flux spectra are independent of atmospheric model parameters [*Fuller-Rowell*

*and Evans*, 1987]. The upper boundary condition of the $O^+$ diffusion equation is determined by the electron density measurements with an assumption that the $O^+$ is the dominate ions at the satellite altitude. The lower boundary condition assumes photochemical equilibrium. The vertical distribution of $NO^+$, $O_2^+$, and $N_2^+$ are obtained using the photochemical equilibrium code developed by *Roble et al* [1987] while the total electron density is determined by the procedures discussed by *Roble and Ridley* [1987].

The global mean model also provides a technique to solve the electron and ion energy equations. The one-dimensional electron energy equation [*Schunk and Nagy*, 1978] is solved by considering photoelectron heating as the main source term and the electron neutral elastic and inelastic collision processes as the main loss terms. The upper boundary condition for this equation is determined by the electron temperature measurement at the satellite altitude. The lower boundary condition is set to be equal to the neutral temperature calculated by the MSIS-90 model. The ion temperature is then calculated by considering the local thermal equilibrium between the ions and neutrals, including the Joule heating specified from the satellite measurements and VSH neutral winds.

The Pedersen and Hall conductivities are determined using the calculated electron and ion densities and temperatures. In order to determine the Joule heating rate, we have used the satellite measured ion drift vector to derive the electric field in a background magnetic field which is measured at the satellite orbit. This electrical field is then assumed to map downward along the magnetic field lines. The neutral wind vector profiles needed in the Joule heating calculation are obtained from the VSH model with measured neutral winds at the satellite orbit used as a guide to adjust this model. Figure 1 shows a schematic block diagram of the extended satellite track model.

## 3. DE-2 Measurements from Orbit 1222

The Dynamics Explorer-2 satellite passed over the southern hemisphere polar cap on orbit 1222 between 0500UT and 0545 UT on October 25, 1981. Simultaneous measurements from a number of instruments carried onboard the satellite are used as input to the satellite track model. The particle spectra are obtained using the Low Altitude Plasma Analyzer , LAPI [*Winningham et al.*, 1981]. The ion drifts are obtained by combining the zonal and meridional components from the Ion Drift Meter, IDM [*Heelis et al.*, 1981], and the Retarding Potential Analyzer, RPA [*Hanson et al.*, 1981] instruments, respectively. The neutral winds are measured by the Fabry-Perot Interferometer, FPI [*Hays et al.*, 1981] and the Wind and Temperature Spectrometer, WATS [*Spencer et al.*, 1981]. In addition to these instruments, the Langmuir Probe, LANG [*Krehbiel et al.*, 1981] and the Neutral Atmosphere Composition

Spectrometer, NACS [*Carignan et al.*, 1981] measure the electron density, temperature and neutral constituent abundance. The magnetic fields are measured by the DE-2 Magnetometer, MAG-B [*Farthing et al.*, 1981].

Figure 2 shows a summary of observed plasma and neutral gas parameters which are plotted as a function of universal time for a DE-2 pass (orbit 1222). As can be seen from the lower left panel, this orbit occurred during relatively active geomagnetic conditions. The *Kp* index was about 5 and the IMF $B_Z$ was southward during the DE-2 pass. The ion drifts for this orbit depict a conventional two-cell pattern with an antisunward velocity of about 500 m/s in the polar cap. The ion drifts are used to determine the electric field in a background magnetic field measured by MAG-B.

The measured neutral winds and ion drifts show close agreement in magnitude and direction throughout the dusk auroral zone and polar cap, but demonstrate larger differences in velocities in the dawn convection channel where the neutral winds move in the opposite direction in the higher latitude regions and respond only moderately to the strong sunward ion flow in the lower latitude region. In response to these large velocity differences, the ion temperature shows large increases (~ 1000 K) in the dawn convection channel. These increases are caused by enhanced frictional heating.

The VSH model of *Killeen et al.* [1987] was used to provide neutral wind profiles below the satellite orbit during an active geomagnetic period. Figure 3 shows a comparison of VSH predicted neutral winds with the satellite measurements. Although there are significant differences in detail, the VSH-calculated winds show sufficient similarity with the satellite measurements (antisunward polar cap flow, bounded by moderate and partially sunward flow in the auroral regions) to provide confidence in their use at lower altitudes. The calculated wind altitude profiles are used in the satellite track model to determine the Joule heating rate.

The MSIS-90 model was used to provide the compositional structure below the satellite orbit. The number densities for $N_2$ and O calculated from the modified MSIS-90 model along the satellite track are plotted in the middle panel of Figure 3 (dashed lines). The DE-2 measurements for these two constituents are also shown in this Figure (solid lines) for the same orbit. In this calculation, we have adjusted the exospheric temperature of the MSIS-90 model so that it can reproduce the neutral temperature measurements at the satellite orbit. This adjusted MSIS-90 model is then used in the satellite track model to derive the compositional structure below the satellite altitude.

The electron precipitation flux along the DE-2 track was measured by LAPI. Figure 4(a) shows the downward electron energy flux averaged over pitch angles from 0° to 90°. These fluxes are detected from the LAPI instrument in the energy range from the 5 eV to 31 keV. The electron flux peaks both in the morning and the evening auroral regions. A large scale

precipitation enhancement exists in the evening auroral zone, while in the morning auroral region there are only two discrete auroral arcs. The energetic electron precipitation in the polar cap is found to be very small. These measured electron flux spectra are used to determine the auroral ionization rate below the satellite orbit as described earlier.

## 4. Model Calculations

The calculated particle ionization rate is shown in Figure 4(b) as a function of altitude in the satellite orbit plane. This ionization rate is derived from the LAPI instrument. Two regions of intense ion production are found in the morning and evening auroral ovals. These enhancements in the ion production rate are mainly caused by the energetic particles that are observed in the auroral regions. Hard electrons have enough energy to penetrate into the lower thermosphere and produce enhanced ionization in the E-region, with maximum rates of $3.0\times10^4$ $cm^{-3}$ and $2.6\times10^4$ $cm^{-3}$ near 115 km in the morning and evening auroral region respectively. The polar cap is characterized by a soft particle drizzle. These particles produce less intense ionization in this region. In addition to this particle ionization, the solar photoionization production rate must be taken into account, since a part of this orbit is in the sunlit polar cap. Figure 4(d) shows the total ionization rate which combines the ion production rate from these two sources. The morning auroral oval is sunlit, therefore solar photoionization dominates most of the ion production in the F-region. Particle precipitation is only important within the E-region where few solar photons penetrate. In the evening auroral zone, however, particle precipitation dominates the total ion production rate at all altitudes below the satellite orbit. Within the polar cap, the ionization rate is controlled by solar photoproduction again. The total ionization rate is used as an input to determine the electron and ion densities in the satellite track model.

Figure 4(c) illustrates the calculated electron density below the satellite orbit. Energetic particles in the auroral region enhance the electron density at lower altitudes (E-region) with a peak electron density of ~$4.4\times10^5$ $cm^{-3}$ at 115 km near 72°S geographic latitude. The electron density in the evening auroral zone is highly irregular due to the dominance of particle precipitation. It is clear that there exists a definite correlation between the enhancement of particle precipitation in the auroral region and the increase of the electron density in the lower thermosphere. In contrast to the particle-dominated auroral regions, the electron distribution in the polar cap is less irregular, increasing with decreasing solar zenith angle.

Electron and ion temperatures are depicted in Figures 5 and 6, respectively. The electron and ion temperatures vary uniformly in the satellite orbit plane except in the auroral regions. Outside the auroral regions, the ion temperature is lower than the electron temperature

indicating that energy is transferred from the electrons to the ions through Coulomb collisions. However, inside the auroral oval, the ion temperature becomes highly structured and can even exceed the electron temperature. This occurs because the ion temperature responds directly to the Joule heating, thus leading to the increase in magnitude.

The electron and ion temperatures and densities discussed above are used to calculate the Hall and Pedersen conductivities. Figures 7(a) and 7(b) show this calculation. The Pedersen conductivity peaks in the region near 125 km, while the Hall conductivity maximizes at lower altitudes between ~100 and 120 km. The precipitating electrons contribute to the large enhancement of the conductivities in the E-region auroral oval. This enhancement is less pronounced in the polar cap, which is dominated by solar photoionization. The height-integrated Hall and Pedersen conductivities are shown in Figure 8. Two peaks for Hall and Pedersen conductivities are found within the morning auroral region near 72°S and 64°S, with maximum values of the Hall conductivity of about 35 mhos. Within the evening auroral oval the height-integrated Hall and Pedersen conductivities have more irregular structures, with amplitudes between 5 and 18 mhos. The height-integrated Hall conductivity is larger than the height-integrated Pedersen conductivity in the auroral regions, reflecting the harder auroral particle precipitation which produces ionization in the lower E-region rather than at higher altitude where Pedersen conductivity dominates.

The calculated Joule heating rates in the satellite orbit plane are shown in Figure 7(d). The largest Joule heating rate occurs in the morning auroral region where large ion drifts are observed (Figure 2). The maximum rate is about $6\times10^{-6}$ ergs/cm$^2$s at 125 km near 67°S. Another enhancement in Joule heating is found in polarward of this auroral region, corresponding to the region of large velocity shear between the neutrals and the ions. The frictional heating resulting from the ion-neutral velocity difference enhances the Joule heating rate, which reaches a peak value of about $10^{-6}$ ergs/cm$^2$s at 125 km. Another enhancement is located in the evening auroral region with a smaller magnitude. The Joule heating rate is smaller in the polar cap than in the auroral zone because the neutral wind moves in the same direction as the ion drift in this region, which reduces the frictional heating rate.

The neutral gas heating rate due to particle precipitation is shown in Figure 7(c). The particle heating rate is obtained by multiplying a neutral heating efficiency for auroral particle precipitation given by *Rees et al.* [1983, Figure 7] to the auroral ionization rate shown in Figure 4(b). Neutral heating efficiency has a value of about 55% up to an altitude of 200-250 km and then decreases above this altitude. The particle heating rate is considerably smaller than the Joule heating rate in most regions below the satellite orbit, but is important in the auroral regions where it can even exceed the Joule heating rate below 100 km. The neutral gas heating

rates discussed here will be used in the next section to study the electrical energy budget below the satellite orbit.

## 5. Poynting Flux and Joule Heating

The study of the electrical energy budget in the lower thermosphere/ionosphere is critically dependent on the electrical energy exchange rate between this region and the magnetosphere. In most cases, the magnetosphere/solar wind dynamo is a source of electrical energy to the high-latitude thermosphere/ionosphere. Some of this energy is dissipated in the lower thermosphere by Joule heating. The rest is converted into neutral mechanical energy through Lorentz energy transfer. The Poynting flux derived at the satellite altitude provides a measure of the net energy flow between the magnetosphere and the thermosphere/ionosphere below the satellite orbit. Recently, *Kelly et al.* [1991] have used the measurements from the HILAT satellite to determine the Poynting flux in the high-latitude thermosphere. They compared the field-aligned Poynting flux with the height-integrated Joule heating rate but made no allowance for neutral wind contributions. *Thayer and Vickrey* [1992] and *Deng et al.* [1993] have studied this concept further by including neutral wind feedback processes. By assuming some spatial homogeneity in the electrodynamics perpendicular to the magnetic field lines, it is found that the field-aligned Poynting flux derived at the spacecraft position is equal to the flux-tube-integrated energy conversion rate below the satellite orbit [*Gary et al.*, 1993;*Thayer and Vickrey* ; 1992]. This energy conversion rate can be determined by the Joule heating rate plus the work done on the neutrals by the Lorentz force (i.e. mechanical energy transfer rate). In this section, we study the relations between the Poynting flux, Joule heating rate and mechanical energy transfer rate.

The Poynting flux is defined by $\mathbf{S} = \mathbf{E}\times\delta\mathbf{B}/\mu_0$, where $\mathbf{E}$ is the electric field measured at the satellite orbit and $\delta\mathbf{B}$ is perturbations of the geomagnetic field measured at the satellite track. The electric field data are derived from the ion velocities measured with the IDM and the RPA. The perturbation magnetic field is obtained as the difference between the magnetic field measured at the DE-2 satellite from MAG-B and a model of the Earth's intrinsic field derived from the Magsat mapping mission of the previous year. The accuracy of this perturbation magnetic field is limited by determining the base line of the Earth's intrinsic field. A several hundred nT deviation of the perturbation field may occur due to the uncertainty in the attitude of the DE-2 spacecraft and the astromast upon which the magnetometer sensor is mounted. To compensate for these errors, a cubic spline was used to determine a new base line. The details of this technique are described by *Gary et al.*[1993]. This fitted curve is assumed to be a realistic base line for the intrinsic magnetic field.

Figure 9 shows the 1 second resolution data for the derived field-aligned Poynting flux along orbit 1222 with a nominal accuracy of 1.0 ergs/cm$^2$s. The flux is entirely downward throughout the pass, with the maximum value of 19.5 ergs/cm$^2$s occurring in the morning auroral oval near 67°S. In the evening auroral zone the flux is relatively small and irregular with an amplitude of about 5 ergs/cm$^2$s. The downward flux indicates that the electromagnetic energy associated with the Poynting flux is transferred from the magnetosphere to the thermosphere.

Figure 10 illustrates the model-calculated height-integrated energy conversion rate below the satellite orbit. This conversion rate is determined by integrating the local energy transfer rate defined as $\mathbf{J}\bullet\mathbf{E}$, where the electrical current $\mathbf{J}$ is calculated by

$$\mathbf{J} = \sigma\bullet(\mathbf{E} + \mathbf{U}\times\mathbf{B})$$

The electrical field $\mathbf{E}$ is derived from the ion drifts and magnetic field measurements along the satellite orbit. We have assumed that this electric field can map down to the lower thermosphere along the magnetic field lines. The neutral wind $\mathbf{U}$ is calculated from the VSH model. A comparison of this neutral wind with the DE-2 measurements at the satellite altitude is shown in Figure 3. The model-calculated energy conversion rate is in good agreement with the measured field-aligned Poynting flux. However, some differences exist in the polar cap where the model underestimates the Poynting flux. The reason for this difference may lie in the underestimation of electron density in the polar cap due to the lack of transport effects in our one dimensional model. The antisunward ion drifts in the polar cap would move the daytime electron density into the nightside ionosphere, resulting in an increase in electron density in the satellite orbit plane which is located near the solar terminator. This transport effect is less pronounced in the auroral regions because the particle-enhanced electron density peaks at lower altitudes where transport is less important. In general, the degree of agreement shown in this comparison gives us confidence in the extended satellite track code, allowing the model to be used to study the relative importance of the Joule heating rate and Lorentz energy transfer rate below the satellite track.

The height-integrated Joule heating rate is shown in Figure 11. The Joule heating rate is similar in magnitude to the energy conversion rate in the auroral regions, indicating that most of the electromagnetic energy imposed from the magnetosphere in these regions is dissipated by Joule heating in the lower thermosphere, and that only a small part of this energy is converted into the neutral mechanical energy through Lorentz energy transfer. Figure 12 shows the ratio of the calculated height-integrated Lorentz energy transfer rate to the height-integrated Joule heating rate. As expected, The contribution of this energy transfer rate is very small in the

auroral regions (about 10%). However, it contributes significantly to the total energy conversion rate in the polar cap and can reach about 40% of the Joule heating rate across most of the polar cap. In this region, the neutral wind can act either as a generator, in which case the neutral wind releases energy and the Lorentz energy transfer rate is negative, or as a load in which case the neutral wind gains energy and the Lorentz energy transfer rate is positive.

## 6. An Overflight of Chatanika Site

In the previous section, we compared our model predictions with the satellite-measured Poynting flux. Another way to test these model predictions is to compare them with ground based observations. An overflight of the incoherent scatter radar facilities at Chatanika (65.1°N, 147.5°W) has provided such an opportunity to carry out a detailed comparison between the model calculations and radar measurements. The geometry of the satellite pass over Chatanika, Alaska is illustrated in Figure 13. For this close conjunction, the satellite was at an altitude of 740 km (orbit 1586), moving along the 146°W meridian at 1635 UT on November 18, 1981. The overflight occurred during southward IMF conditions, with a *Kp* of $3^+$.

The electron flux spectra measured by the LAPI instrument on the DE-2 satellite at 1634:56 UT is displayed in Figure 14. This measurement was taken in the auroral regions where particle precipitation is strong. At this time the satellite was at about the geographic latitude of Chatanika but was about 2° off in longitude. The data were averaged over 8 seconds, which covers about 64 km. The variability of the spectra shape at different pitch angles is relatively small, thus implying an isotropic distribution. The maximum electron flux is about $10^7$ (1/cm2-s-ev-str) at lower energy. At higher energy, there is a small increase in hard auroral electron precipitation near 1 kev. Overall, the flux observed in this orbit is softer and less intense than that typically observed in auroral arcs. An average of this spectra over six pitch angles is used as an input to our model for determining the ionospheric structure below the satellite. For this calculation, we assumed that the observed electron flux was present for a sufficiently long time for a steady state electron density profile to be reached. The other inputs include the electron density and temperature measured by DE-2. Unfortunately, the neutral temperature measurement is not available for this period. We have used the satellite-measured O density as a guide to adjust the exospheric temperature in the MSIS-90 model so that it can reproduce the O density at the satellite orbit. Another uncertainty is the ion drifts which are also not available for this orbits. They are replaced by the radar measurements at an altitude close to the satellite orbit.

The incoherent scatter radar at Chatanika, Alaska was making measurements during this overflight. The basic physical parameters measured by the radar are the electron density,

electron and ion temperatures, and the plasma velocity along the line of sight of the radar beam. Data was obtained from 60 km to about 500 km during this experiment. A detailed description of the equipment and the measurement capabilities of the radar is given by *Leadabrand et al.* [1972].

The overflight occurred on November 18, 1981. In this experiment, the antenna was held at 70° elevation and the returned signals were averaged for 3 minutes each at three consecutive azimuths that are 120° apart. The ion drift velocity is obtained by combining the line of sight velocities measured from these three azimuths. A long pulse was used for the velocity and temperature measurements and data were obtained at eight altitudes, starting at about 103 km and spaced 50 km apart. For the electron density measurements, a separate short (60 μsec) pulse was used, which gives an altitude resolution of about 9 km. The conductivities and Joule heating are derived by using a neutral atmosphere model and neglecting the neutral winds

Figure 15 shows a comparison of our satellite track model-calculated electron density profile with the radar measurement during the overflight (1635 UT). The solid line indicates the radar measurements between 1629 and 1642 UT. The dashed line is calculated from the satellite track model using the DE-2 measurements at 1635 UT, about $2^0$ in longitude to the east of Chatanika. The satellite track model overestimates the electron density in the F-region, while it underestimates the electron density in the E-region. At high altitudes, the data agree well with the model predictions, indicating that the boundary condition determined by the satellite is close to the radar measurement. This overflight happened in the early morning (solar local time 0706), so the solar zenith angle at E-region altitudes was large. Therefore, the observed enhancement of E-region electron density is mainly caused by energetic particle precipitation. Our model reproduces this increase quite well although it underestimates the magnitude. This underestimation may be caused by the use of a neutral atmosphere model, which has limited accuracy in the auroral regions during active geomagnetic conditions. It may also be explained by the changes of minor neutral constituents such as NO. In our model, we have only used the global mean value of the NO density. However, the NO density will increase significantly from its mean level in the auroral region due to the increases in the $N_2$ dissociation rate resulting from intense particle precipitation [*Roble*, 1992].

In the F-region, the model electron density is substantially higher (about 50%) than that of the radar measurements. Several factors contribute to this disagreement. First, as the altitude increases, horizontal transport effects become important. Since this overflight occurred on the equatorial side of the morning auroral oval, the convection is more likely to be in the sunward direction. The transport effect therefore would tend to move the lower electron density in the dark ionosphere into the morning auroral region, resulting in a decrease in electron

density in this region. A 1D model cannot include this effect and should therefore lead to an overestimation of the electron density. Another contributing factor is time dependent effects of the auroral event. As discussed by *Rees et al.* [1980], an auroral event is a time dependent process in which various ion species respond to particle bombardment at different rates. To model this process rigorously requires a knowledge of the time history of the precipitation electron flux. It is possible that a steady state is not reached at the time of the overflight due to the sluggish response of the F-region ionization. As a result, the electron density remains lower than that in the steady state, where it has higher value due to the decrease in the electron temperature. Finally, the 2° longitudinal offset of the satellite pass over the Chatanika site may also contribute to this disagreement. Overall, despite the discrepancy between the experimental result and our model calculation, there is a good general agreement as to the morphology of the electron density profile.

The comparison of electron temperatures is shown in Figure 16. While crude agreement in shape is seen, a significant difference between the radar-measured temperatures (solid line) and the modeled temperatures (dashed line) of ~400 K exists at the upper altitudes, with the modeled temperatures being higher than the radar measurements. Since the satellite measurement is used as the upper boundary condition for the satellite track code, this discrepancy may account for some of the disagreement at lower altitudes. It is impossible to determine whether instrumental effects or spatial changes in the electron temperature distribution are responsible for the discrepancy. The ion temperatures are illustrated in Figure 17. The model overestimates the ion temperature in the region below 300 Km by as much as 400 K. Since the ion temperature is closely coupled with the neutral temperature in this region, most of difference is due to the overestimation of neutral temperature in the F-region below the satellite orbit.

The comparison of radar-measured and modeled Hall and Pedersen conductivities are depicted in Figures 18 and 19, respectively. There is a good agreement between the model calculations and the radar measurements, indicating that the satellite track model has an ability to determine the conductivities in the lower thermosphere with reasonable accuracy. Finally, we present a comparison between radar-derived Joule heating rates and the model calculation in Figure 20. As expected, good agreement is attained in the lower thermosphere. The difference at the higher altitudes is mainly caused by the overestimation of the electron density. Since the Joule heating peaks in the lower thermosphere and decreases rapidly with increasing altitude, this disagreement does not have a significant effect on the height-integrated Joule heating rate (the value of height-integrated Joule heating rate are about 1.38 and 1.51 ergs/cm$^2$-s, calculated from radar measurements and model predictions respectively).

## 7. Summary

We have developed a satellite track model. The major model inputs are measurements of the electron precipitation flux to determine ionization rates and of ion drifts to determine the Joule heating rates. The model has been used to study the ionospheric structure below the satellite pass (orbit 1222) and has been compared with the incoherent scatter radar measurements at Chatanika, Alaska during a DE-2 overflight. Our principal results may be listed as follows:

1. The auroral particle precipitation plays an important role in determining the structure of the high latitude ionosphere/thermosphere, especially in the lower thermosphere.

2. The model has demonstrated an ability to map the DE-2 satellite measurements into the lower thermosphere/ionosphere.

3. A good first-order agreement has been reached between the DE-2 derived field-aligned Poynting flux and the height-integrated energy conversion rate, yielding confidence in the calculated lower thermospheric conductivities and Joule heating rates.

4. The study of electromagnetic energy budget below the satellite orbit indicates that most of the electric energy from the magnetosphere is dissipated by Joule heating in the auroral region. Only a small part is converted into the neutral wind mechanical energy in this region. However, the neutral wind contributes significantly to the electromagnetic energy budget in the polar cap.

5. Comparison with the radar measurements suggests that the model is able to determine the conductivities and Joule heating rate in the lower thermosphere with a reasonable accuracy, but it cannot reproduce the details of all the experimental measurements.

Acknowledgment:

This study was supported by NASA grant NAGW-3457 and NAG5-465, by NSF grant ATM-8918476 and ATM-9096134, and USAF grant F19628-89-K-0026 to the University of Michigan. The study also made use of the CEDAR data base at NCAR, which, along with Chatanika radar, is supported by the National Science Foundation. The authors are

grateful to W. B. Hanson, R. A. Heelis, and J. A. Slavin for providing their DE-2 data. We also would like to thank Dr. R. A. Heelis for useful discussions and suggestions.

List of the Figures

Figure 8 The height-integrated Hall conductivity (dashed line) and Pedersen conductivity (solid line) in [mho] along satellite orbit 1222.

Figure 9 The field-aligned Poynting flux along satellite orbit 1222, this flux is derived from the DE-2 measurements.

Figure 10 The model calculated height-integrated energy conversion rate for satellite orbit 1222.

Figure 11 The same as Figure 10 except for height-integrated Joule heating rate.

Figure 12 The ratio of height-integrated mechanical energy transfer rate to the height-integrated Joule heating for satellite orbit 1222.

Figure 13 Satellite track at 740 km altitude during the overflight of Chatanika, Alaska, on November, 18, 1981.

Figure 14 Eight-second average of electron spectra measured by the LAPI instrument around 1634:56 UT on November, 18, 1981.

Figure 15 Comparison of radar measured electron density profile (solid line) with the model calculations (dashed line) during the overflight at 1635 UT.

Figure 16 The same as Figure 15 except for the electron temperature.

Figure 17 The same as Figure 15 except for the ion temperature.

Figure 18 Comparison of derived Hall conductivity (solid line) from the radar measurement with the model calculation (dash line) at the overflight.

Figure 19 The same as Figure 18 except for the Pedersen conductivity.

Figure 20 The same as Figure 18 except for the Joule heating rate.

References

Carignan, G. R., B. P. Block, J. C. Maurer, A. E. Hedin, C. A. Reber, and N. W. Spencer, The Neutral Mass Spectrometer on Dynamics Explorer, *Space Space Instrum.*, *5*, 429-442, 1981.

Deng, W., T.L. Killeen, A.G. Burns, R.G. Roble, J, Slavin, and L.E. Wharton, The effects of neutral inertia on ionospheric currents in the high latitude thermosphere following a geomagnetic storm, *J. Geophys. Res. 98,* 7775-7790, 1993.

Emery, B. A., R. G. Roble, E. C. Ridley, T. L. Killeen, M. H. Rees., J. D. Winningham, G. R. Carignan, P. B. Hays, R. A. Heelis, W. B. Hanson, N. W. Spencer, L. H. Brace and M. Sugiura, Thermospheric and Ionospheric Structure of the Southern Hemisphere Polar Cap on October 21, 1981, as Determined From Dynamics Explorer 2 Satellite Data, *J. Geophys. Res.*, *90*, 6553-6566, 1985.

Farthing, W. H., M. Sugiura, B. G. Ledley, and L. J. Cahill, Jr., Magnetic field observations on DE-A and -B, *Space Space Instrum.*, *5*, 551-560, 1981.

Foster, J., An empirical electric field model derived from Chatanika radar data, *J. Geophys. Res.*, *88*, 981-987, 1983a.

Foster, J. C., J.-P. St.-Maurice and V. J. Abreu, Joule heating at high latitudes, *J. Geophys. Res.*, *88*, 4885-4896, 1983b.

Fuller-Rowell, T. J., and D. S. Evans, Height integrated Pedersen and Hall conductivity patterns inferred from the TIROS-NOAA satellite data, *J. Geophys. Res 92.*, 7606-7618, 1987.

Gary, J. B., R.A. Heelis, W. B. Hanson and J. A. Slavin, Examples of Poynting vector determination using DE-B satellite data, *J. Geophys. Res.*, *89*, in press, 1993.

Hanson, W. B., R. A. Heelis, R. A. Power, C. R. Lippincott, D. R. Zuccaro, B. J. Holt, L. H. Harmon, and S. Sanatani, The Retarding Potential Analyzer for Dynamics Explorer-B, *Space Sci. Instrum.*, *5*, 503-510, 1981.

Hays, P. B., T. L. Killeen, and B. C. Kennedy,The Fabry-Perot Interferometer on Dynamics Explorer, *Space Space Instrum.*, *5*, 395-416, 1981.

Hays, P. B., T. L. Killeen, N. W. Spencer, L. E. Wharton, R. G. Roble, B. E. Emery, T. J. Fuller-Rowell, D. Rees, L. A. Frank, and J. D. Craven, Observations of the dynamics of the polar thermosphere, *J. Geophys. Res.*, *89*, 5597-5612, 1984.

Heelis, R. A., W. B. Hanson, C. R. Lippincott, D. R. Zuccaro, L. H. Harmon, B. J. Holt, J. E. Doherty, and R. A. Power, The Ion Drift Meter for Dynamics Explorer-B, *Space Space Instrum.*, *5*, 511-522, 1981.

Heelis, R. A., J. K. Lowell, and R. W. Spiro, A model of the high-latitude ionospheric convection pattern, *J. Geophys. Res.*, *87*, 6339-6345, 1982.

Heelis, R. A. and W. R. Coley, Global and local Joule heating effects seen by DE-2, *J. Geophys. Res.*, *93*, 7551-7557, 1988.

Heppner, J. P., Empirical models of high-latitude electric fields, *J. Geophys. Res.*, *82*, 1115-1125, 1977.

Kelley, M. C., D. J. Knudsen and J. F. Vickery, Poynting flux measurements on a satellite: A diagnostic tool for space research, *J. Geophys. Res.*, *96*, 201-207, 1991.

Killeen, T. L., R. W. Smith, N. W. Spencer, J. W. Meriwether, D. Rees, G. Hernandez, P. B. Hays, L. L. Cogger, D. P. Sipler, M. A. Biondi and C. A. Tepley, Mean neutral circulation in the winter polar F region, *J. Geophys. Res.*, *91*, 1633-1649, 1986.

Killeen, T. L., R. G. Roble, and N. W. Spencer, A computer model of global thermospheric winds and temperatures, *Adv. Space Res 7.*, 207-215, 1987

Killeen, T. L. and R. G. Roble, Thermosphere Dynamics driven by magnetospheric sources: contributions from the first five years of the Dynamics Explorer program, *Rev. Geophys. Space Phys.*, 329-367, 1988.

Krehbiel, J. P., L. H. Brace, R. F. Theis, W. H. Pinkus, and R. B. Kaplan, The Dynamics Explorer Langmuir Probe Instrument, *Space Space Instrum.*, *5*, 493-502, 1981.

Leadabrand, M. J. Baron, J. Petriceks and H. F. Bates, Chatanika, Alaska, auroral-zone incoherent-scatter facility, *Radio Science 7*, 747-756, 1972.

Rees, M. H., R. G. Roble, J. Kopp, V. J. Abreu, L. H. Brace, H. C. Brinton, R. A. Heelis, R. A. Hoffman, D. C. Kayser, and D. W. Rusch, The spatial-temporal ambiguity in auroral modeling, *J. Geophys. Res.*, *85*, 1235-1245, 1980.

Rees, M. H., B. A. Emery, R. G. Roble, and K. Stamnes, Neutral and ion gas heating by auroral electron precipitation, *J. Geophys. Res.*, *88*, 6289-6300, 1983

Richmond, A. D. and Y. Kamide, Mapping electrodynamic features of the high-latitude ionosphere from localized observations: Technique, *J. Geophys. Res.*, *93*, 5741-5759, 1988.

Roble, R. G., B. A. Emery, R. E. Dickinson, E. C. Ridley, T. L. Killeen, P. B. Hays, G. R. Carignan, and N. W. Spencer, Thermospheric circulation, temperature and compositional structure of the southern hemisphere polar cap during October-November, 1981, *J. Geophys. Res.*, *89*, 9057-9068, 1984.

Roble, R. G., E. C. Ridley and R. E. Dickinson, On the global mean structure of the thermosphere, *J. Geophys. Res.*, *92*, 8745-8758, 1987.

Roble, R. G., and E. C. Ridley, An auroral model of the NCAR thermospheric general circulation model (TGCM), *Annales Geophysicae, 5A, (6)*, 369-382, 1987.

Roble, R. G., and R. E. Dickinson, How will changes in carbon dioxide and methane modify the mean structure of the mesosphere and thermosphere?, *Geophys. Res. Lett., 16*, 1441-1444, 1989

Roble, R. G., The polar lower thermosphere, *Planet. Space Sci. 40*, 271-297, 1992.

Schunk, R. W., and A. F. Nagy, Electron temperature in the F region of the ionosphere: Theory and observation, *Rev. Geophys., 16*, 355, 1978.

Spencer, N. W., L. E. Wharton, H. B. Niemann, A. E. Hedin, G. R. Carignan, and J. C. Maurer, The Dynamics Explorer Wind and Temperature Spectrometer, *Space Space Instrum., 5*, 417-428, 1981.

Thayer, J. P. and J. F. Vickrey, On the contribution of thermospheric neutral wind to high latitude energetics, *Geophys. Res. Lett., 19*, 265-268, 1992

Wallis, D. D. and E. E. Budzinski, Empirical models of height-integrated conductivity, *J. Geophys. Res., 86*, 125-137, 1981.

Winningham, J. D., J. L. Burch, N. Eaker, V. A. Blevins, and R. A. Hoffman, The Low Altitude Plasma Instrument (LAPI), *Space Space Instrum., 5*, 465-476, 1981.

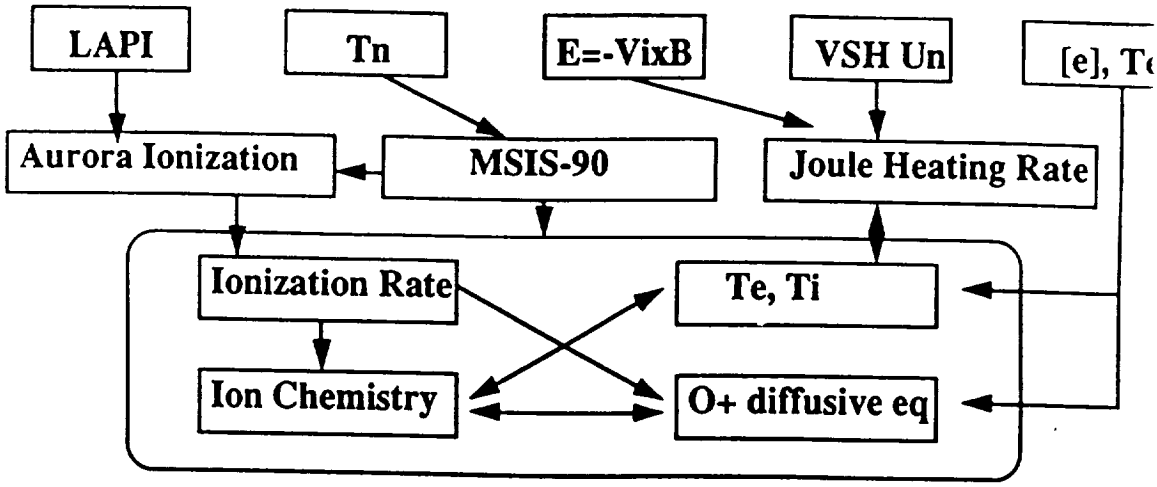
LAPI
Tn
E=-VixB
VSH Un
[e], Te
Aurora Ionization
MSIS-90
Joule Heating Rate
Ionization Rate
Te, Ti
Ion Chemistry
O+ diffusive eq

Figure 1

# DE-2 FPI/WATS/RPA/IDM/NACS/LANG

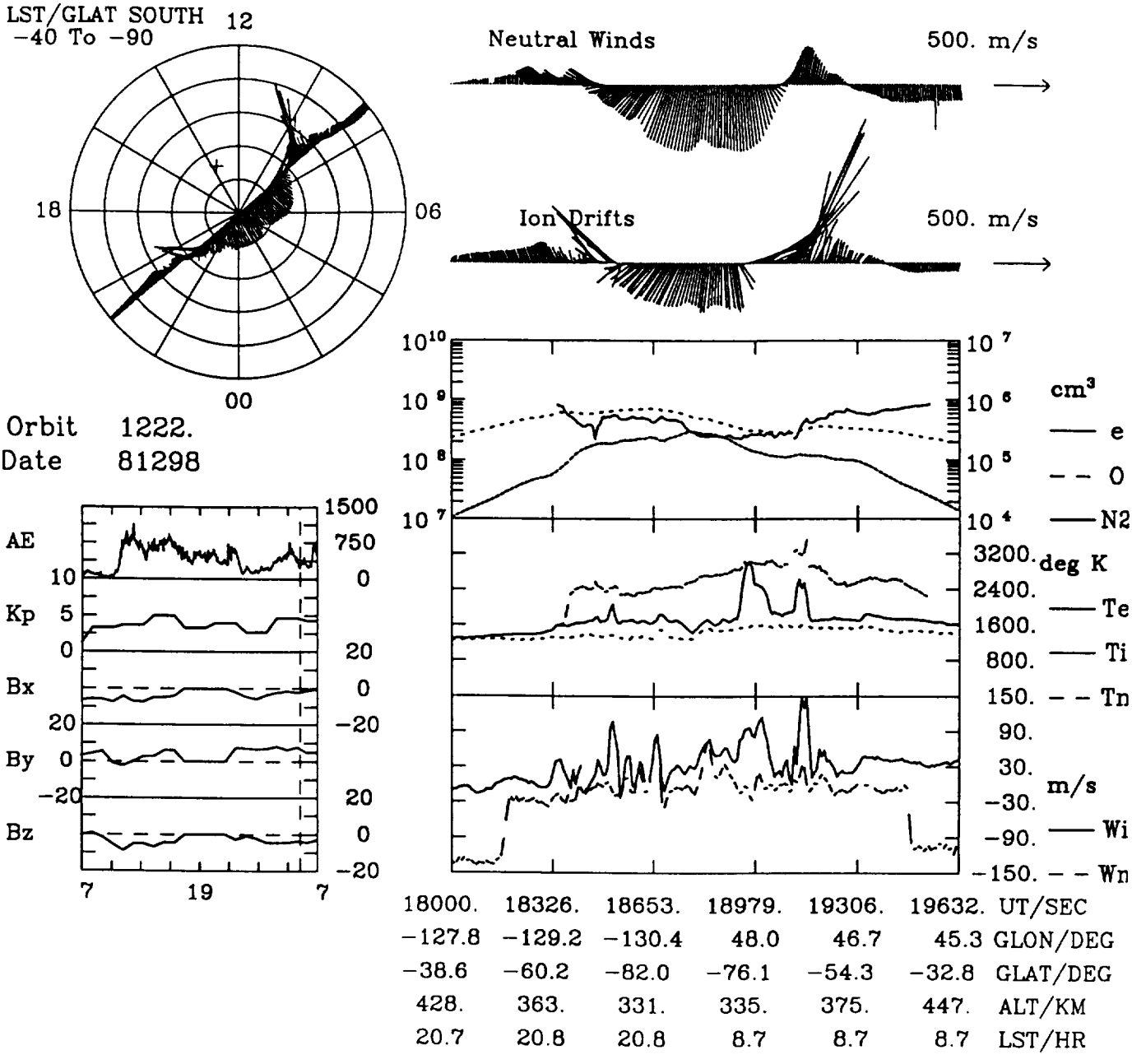


Figure 3

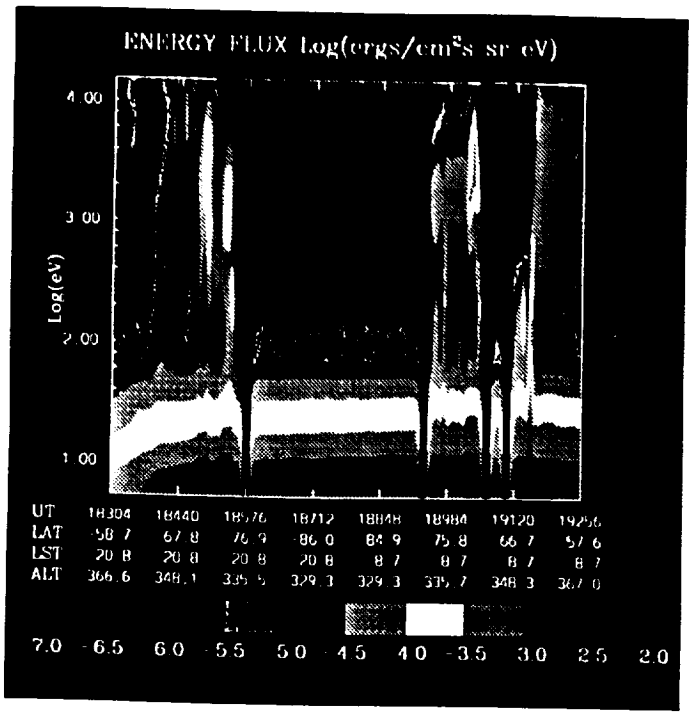
ENERGY FLUX Log(ergs/cm²s sr eV)
Log(eV)
4.00
3.00
2.00
1.00
UT 18304 18440 18576 18712 18848 18984 19120 19256
LAT -58.7 -67.8 -76.9 -86.0 84.9 75.8 66.7 57.6
LST 20.8 20.8 20.8 20.8 8.7 8.7 8.7 8.7
ALT 366.6 348.1 335.5 329.3 329.3 335.7 348.3 367.0
7.0 6.5 6.0 5.5 5.0 4.5 4.0 3.5 3.0 2.5 2.0

(a)

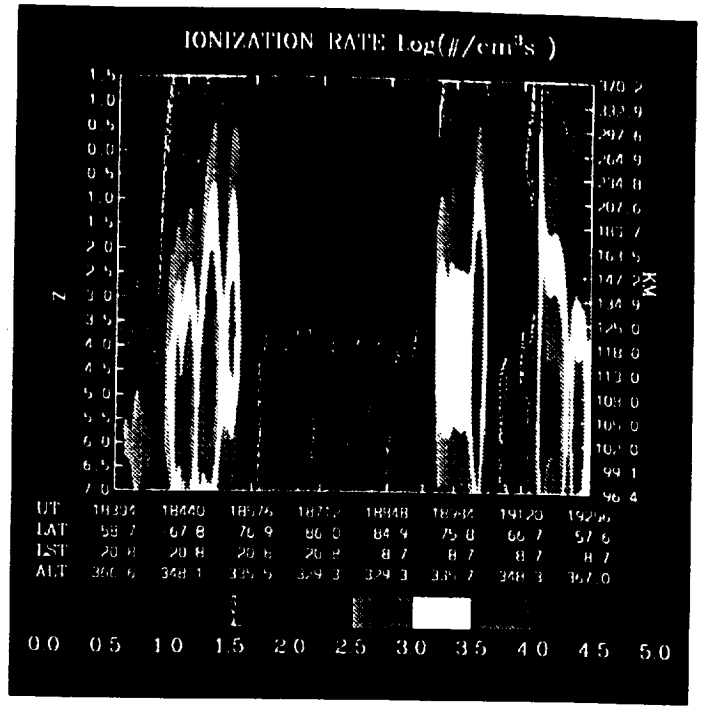
IONIZATION RATE Log(#/cm³s )
Z
KM
UT 18304 18440 18576 18712 18848 18984 19120 19256
LAT -58.7 -67.8 -76.9 -86.0 84.9 75.8 66.7 57.6
LST 20.8 20.8 20.8 20.8 8.7 8.7 8.7 8.7
ALT 366.6 348.1 335.5 329.3 329.3 335.7 348.3 367.0
0.0 0.5 1.0 1.5 2.0 2.5 3.0 3.5 4.0 4.5 5.0

(b)

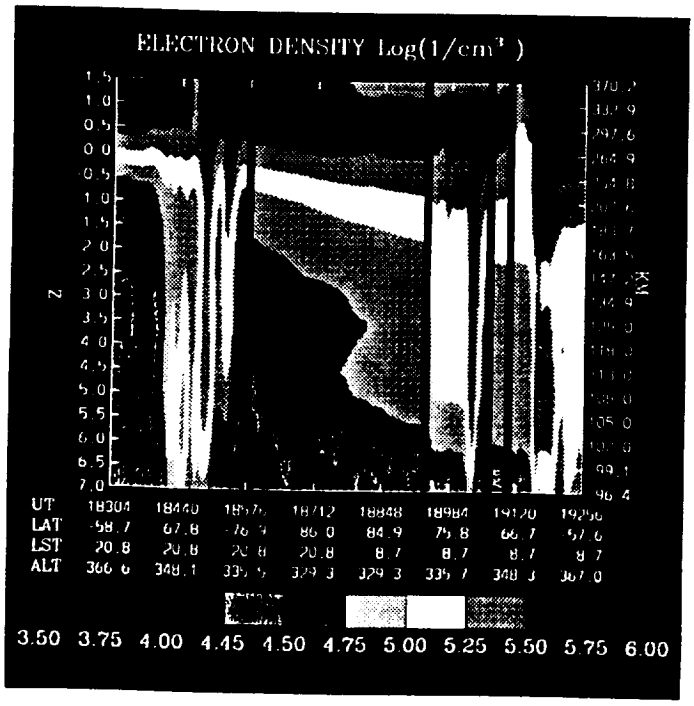
ELECTRON DENSITY Log(1/cm³ )
Z
KM
UT 18304 18440 18576 18712 18848 18984 19120 19256
LAT -58.7 -67.8 -76.9 -86.0 84.9 75.8 66.7 57.6
LST 20.8 20.8 20.8 20.8 8.7 8.7 8.7 8.7
ALT 366.6 348.1 335.5 329.3 329.3 335.7 348.3 367.0
3.50 3.75 4.00 4.45 4.50 4.75 5.00 5.25 5.50 5.75 6.00

(d)

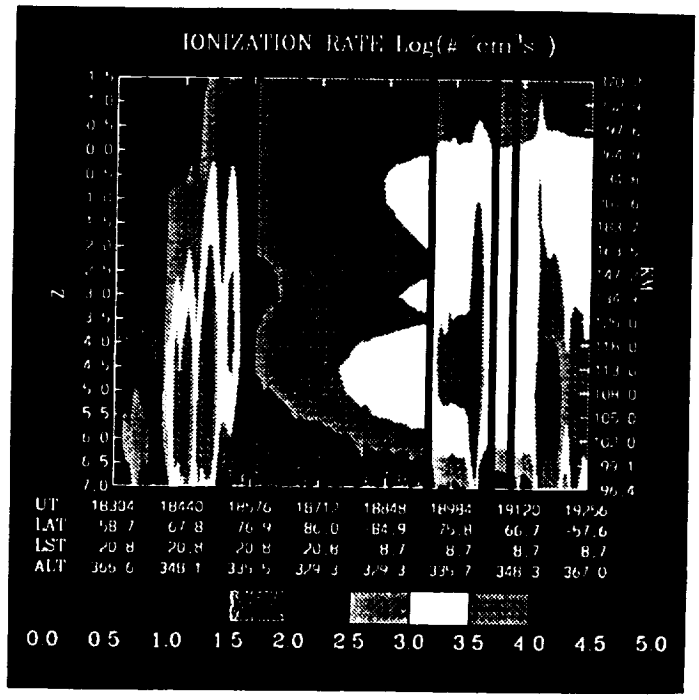
IONIZATION RATE Log(# cm³s )
Z
KM
UT 18304 18440 18576 18712 18848 18984 19120 19256
LAT -58.7 -67.8 -76.9 -86.0 84.9 75.8 66.7 57.6
LST 20.8 20.8 20.8 20.8 8.7 8.7 8.7 8.7
ALT 366.6 348.1 335.5 329.3 329.3 335.7 348.3 367.0
0.0 0.5 1.0 1.5 2.0 2.5 3.0 3.5 4.0 4.5 5.0

(c)

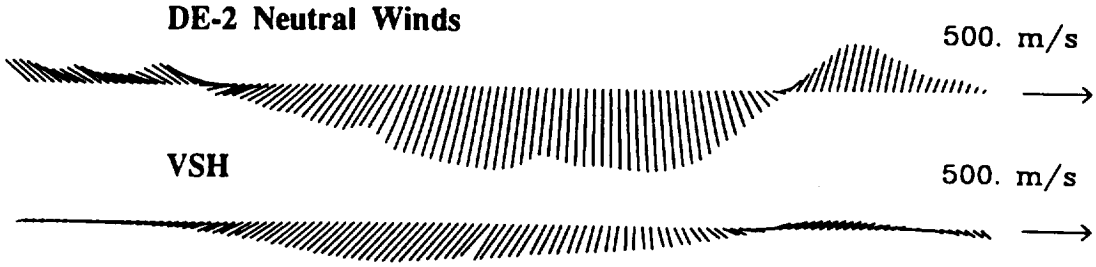


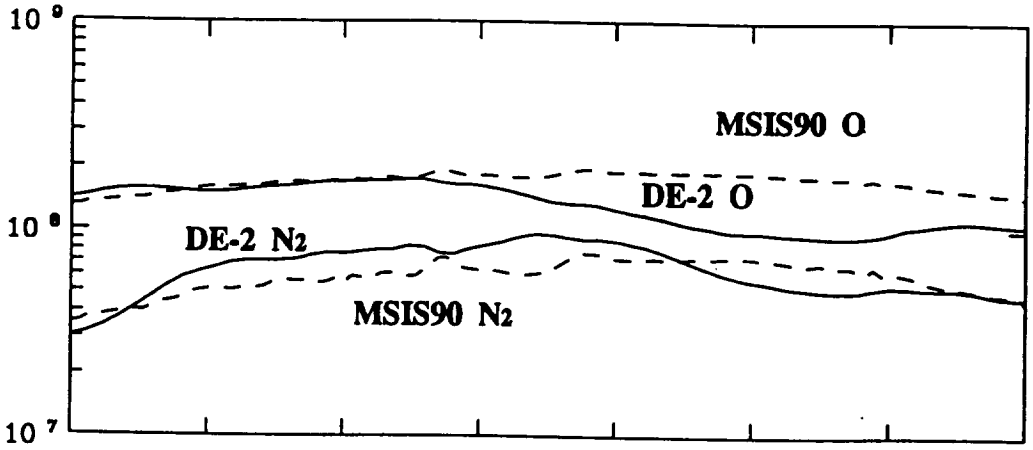


| | | | | | | | |
|---|---|---|---|---|---|---|---|
| 18304 | 18440 | 18576 | 18712 | 18848 | 18984 | 19120 | 19256 UT/SEC |
| −58.7 | −67.8 | −76.9 | −86.0 | −84.9 | −75.8 | −66.7 | −57.6 GLAT/DEG |
| 20.8 | 20.8 | 20.8 | 20.8 | 8.7 | 8.7 | 8.7 | 8.7 LST/HR |
| 366.6 | 348.1 | 335.5 | 329.3 | 329.3 | 335.7 | 348.3 | 367.0 ALT/KM |

ELECTRON TEMPERATURE K

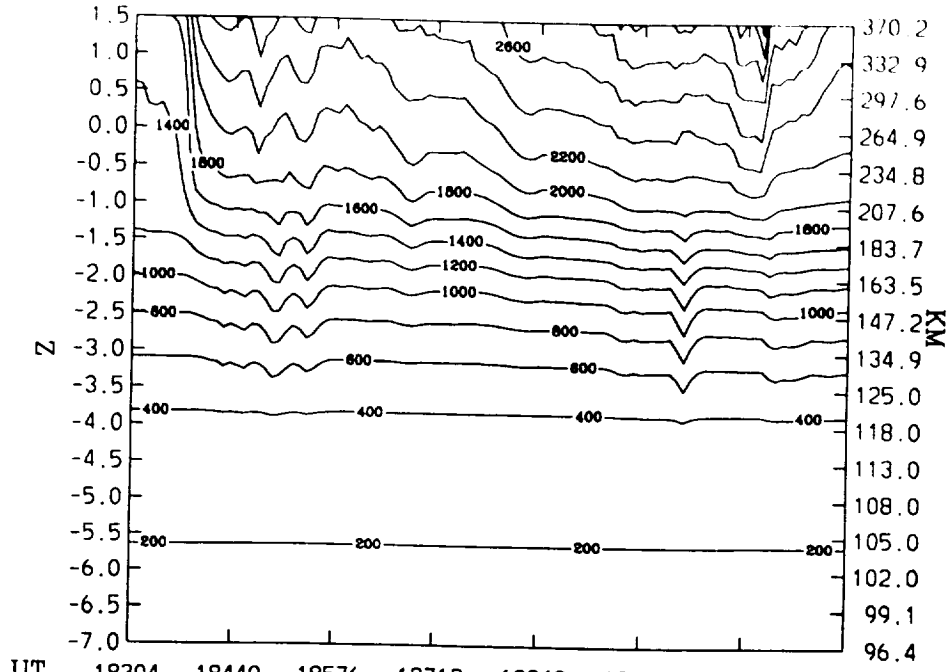


| | | | | | | | | |
|---|---|---|---|---|---|---|---|---|
| UT | 18304 | 18440 | 18576 | 18712 | 18848 | 18984 | 19120 | 19256 |
| LAT | -58.7 | -67.8 | -67.8 | -86.0 | -84.9 | -75.8 | -66.7 | -57.6 |
| LST | 20.8 | 20.8 | 20.8 | 20.8 | 8.7 | 8.7 | 8.7 | 8.7 |
| ALT | 366.6 | 348.1 | 348.1 | 329.3 | 329.3 | 335.7 | 348.3 | 367.0 |

Figure 5

ION TEMPERATURE K

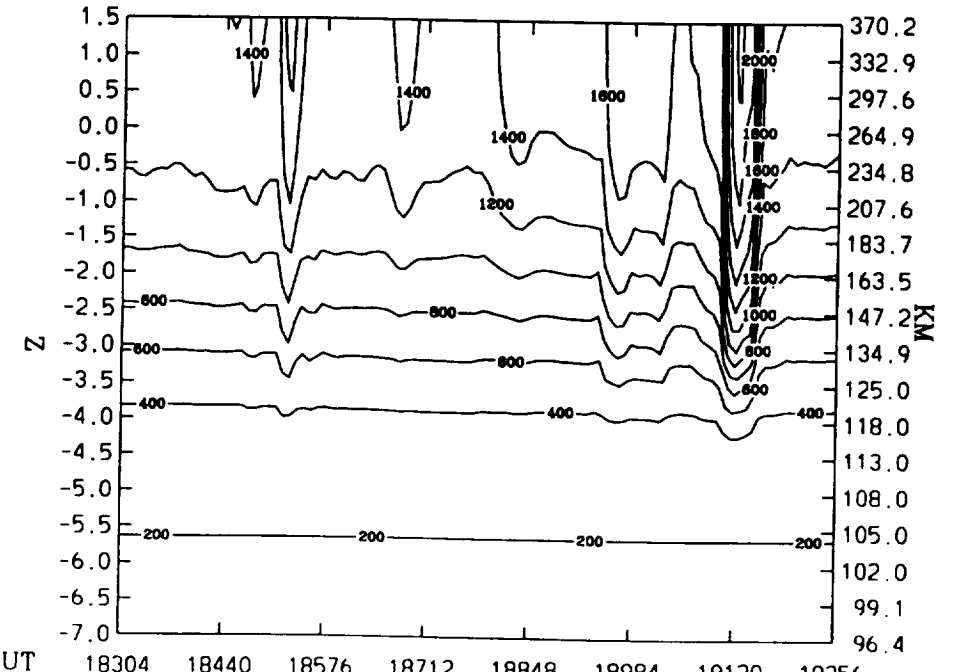


| | | | | | | | | |
|---|---|---|---|---|---|---|---|---|
| UT | 18304 | 18440 | 18576 | 18712 | 18848 | 18984 | 19120 | 19256 |
| LAT | -58.7 | -67.8 | -67.8 | -86.0 | -84.9 | -75.8 | -66.7 | -57.6 |
| LST | 20.8 | 20.8 | 20.8 | 20.8 | 8.7 | 8.7 | 8.7 | 8.7 |
| ALT | 366.6 | 348.1 | 348.1 | 329.3 | 329.3 | 335.7 | 348.3 | 367.0 |

Figure 6

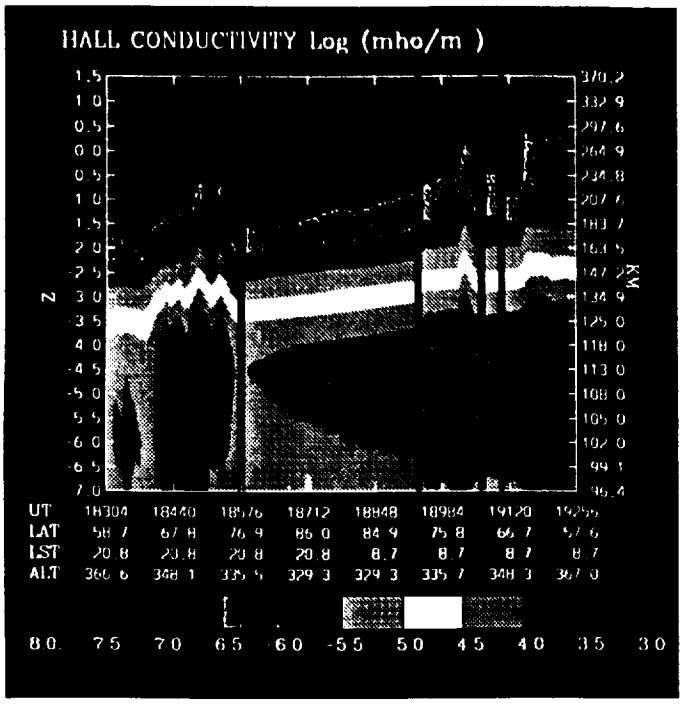
HALL CONDUCTIVITY Log (mho/m )
Z
KM
UT 18304 18440 18576 18712 18848 18984 19120 19256
LAT 58.7 67.8 76.9 86.0 84.9 75.8 66.7 57.6
LST 20.8 20.8 20.8 20.8 8.7 8.7 8.7 8.7
ALT 366.6 348.1 335.5 329.3 329.3 335.7 348.3 367.0
80 75 70 65 60 55 50 45 40 35 30

(a)

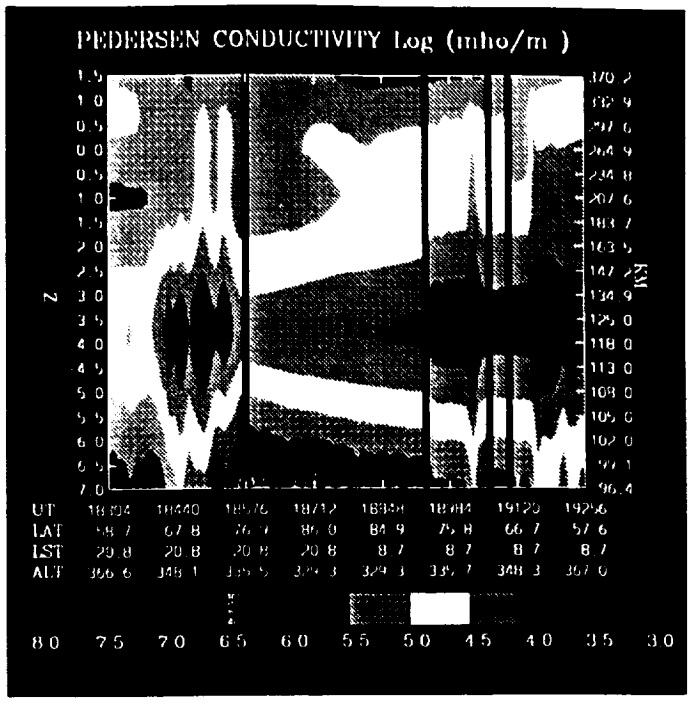
PEDERSEN CONDUCTIVITY Log (mho/m )
Z
KM
UT 18304 18440 18576 18712 18848 18984 19120 19256
LAT 58.7 67.8 76.9 86.0 84.9 75.8 66.7 57.6
LST 20.8 20.8 20.8 20.8 8.7 8.7 8.7 8.7
ALT 366.6 348.1 335.5 329.3 329.3 335.7 348.3 367.0
80 75 70 65 60 55 50 45 40 35 30

(b)

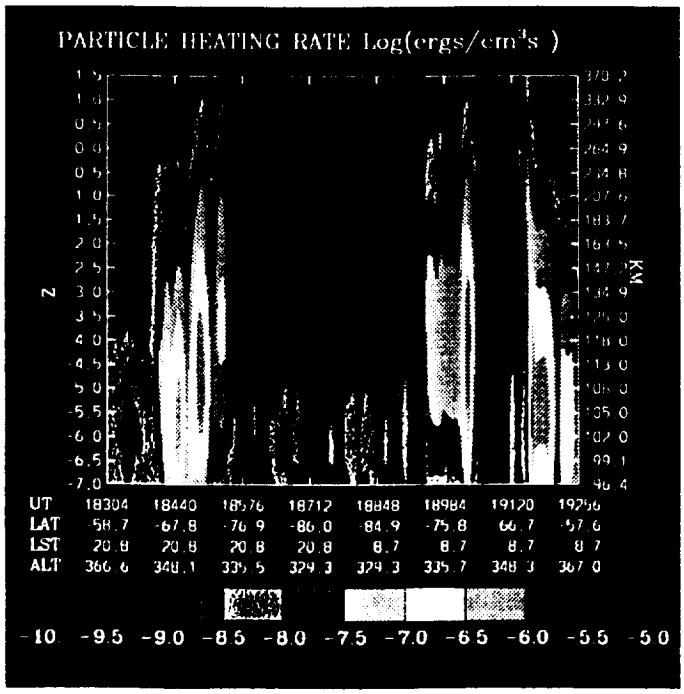
PARTICLE HEATING RATE Log(ergs/cm³s )
Z
KM
UT 18304 18440 18576 18712 18848 18984 19120 19256
LAT -58.7 -67.8 -76.9 -86.0 -84.9 -75.8 66.7 -57.6
LST 20.8 20.8 20.8 20.8 8.7 8.7 8.7 8.7
ALT 366.6 348.1 335.5 329.3 329.3 335.7 348.3 367.0
-10 -9.5 -9.0 -8.5 -8.0 -7.5 -7.0 -6.5 -6.0 -5.5 -5.0

(d)

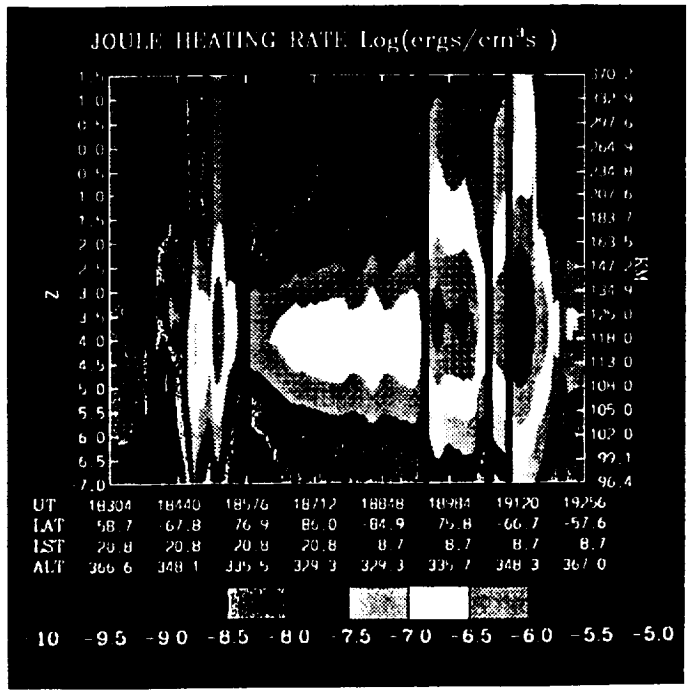
JOULE HEATING RATE Log(ergs/cm³s )
Z
KM
UT 18304 18440 18576 18712 18848 18984 19120 19256
LAT 58.7 67.8 76.9 86.0 84.9 75.8 66.7 57.6
LST 20.8 20.8 20.8 20.8 8.7 8.7 8.7 8.7
ALT 366.6 348.1 335.5 329.3 329.3 335.7 348.3 367.0
10 -9.5 -9.0 -8.5 -8.0 -7.5 -7.0 -6.5 -6.0 -5.5 -5.0

(c)

HEIGHT INTEGRATED CONDUCTANCE

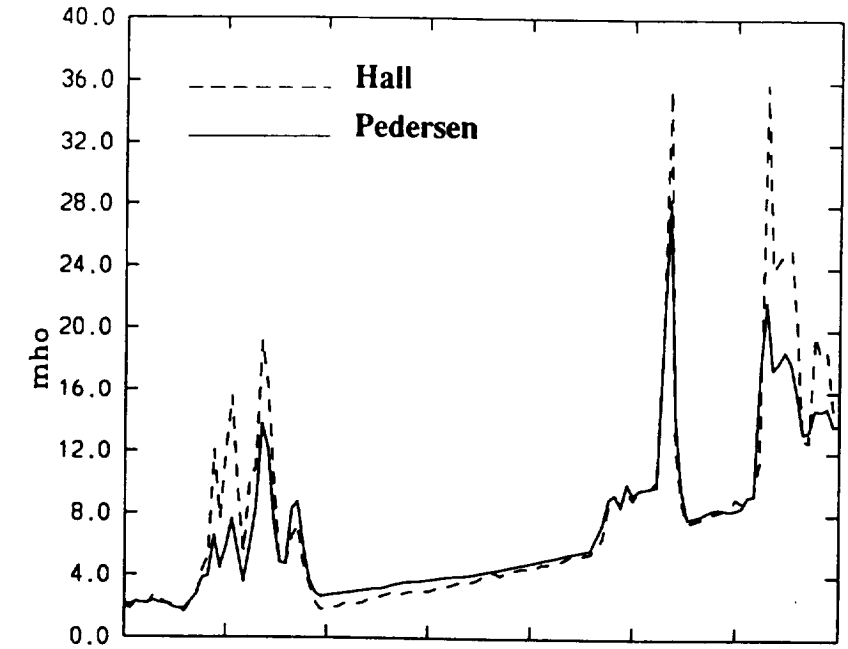


| | | | | | | | | |
|---|---|---|---|---|---|---|---|---|
| UT | 18304 | 18440 | 18576 | 18712 | 18848 | 18984 | 19120 | 19256 |
| LAT | -58.7 | -67.8 | -67.8 | -86.0 | -84.9 | -75.8 | -66.7 | -57.6 |
| LST | 20.8 | 20.8 | 20.8 | 20.8 | 8.7 | 8.7 | 8.7 | 8.7 |
| ALT | 366.6 | 348.1 | 348.1 | 329.3 | 329.3 | 335.7 | 348.3 | 367.0 |

Figure 6

## Field-Aligned Poynting Flux

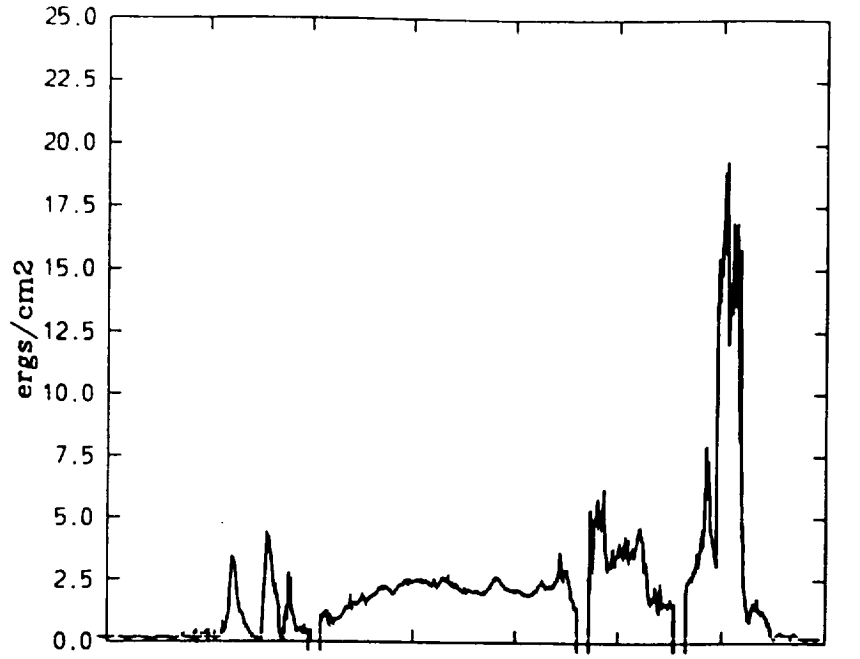


| | | | | | | | | |
|---|---|---|---|---|---|---|---|---|
| UT | 18304 | 18440 | 18576 | 18712 | 18848 | 18984 | 19120 | 19256 |
| LAT | -58.7 | -67.8 | -67.8 | -86.0 | -84.9 | -75.8 | -66.7 | -57.6 |
| LST | 20.8 | 20.8 | 20.8 | 20.8 | 8.7 | 8.7 | 8.7 | 8.7 |
| ALT | 366.6 | 348.1 | 348.1 | 329.3 | 329.3 | 335.7 | 348.3 | 367.0 |

Figure 9

## Height-Intrgrated Energy Conversion Rate

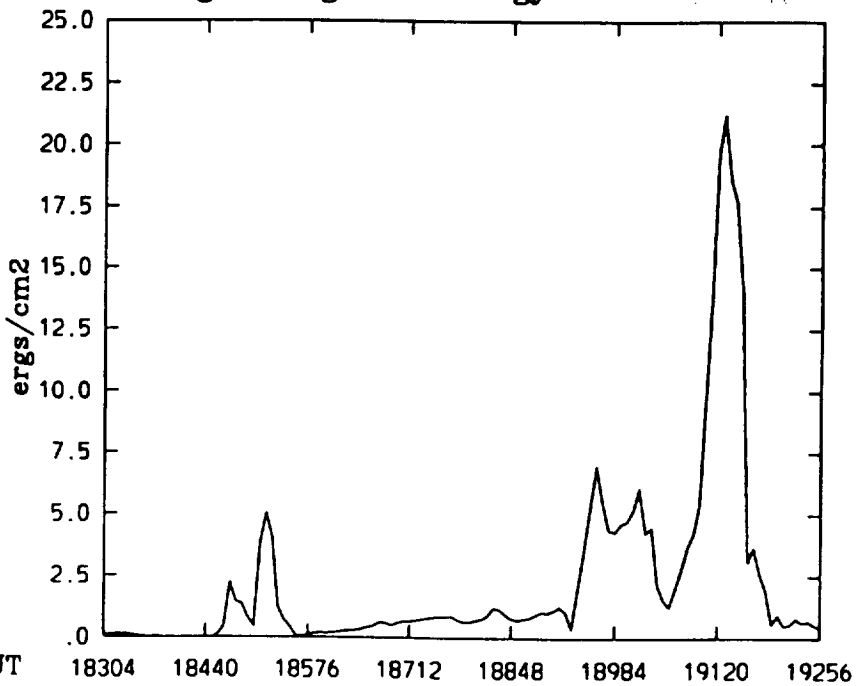


| | | | | | | | | |
|---|---|---|---|---|---|---|---|---|
| UT | 18304 | 18440 | 18576 | 18712 | 18848 | 18984 | 19120 | 19256 |
| LAT | -58.7 | -67.8 | -67.8 | -86.0 | -84.9 | -75.8 | -66.7 | -57.6 |
| LST | 20.8 | 20.8 | 20.8 | 20.8 | 8.7 | 8.7 | 8.7 | 8.7 |
| ALT | 366.6 | 348.1 | 348.1 | 329.3 | 329.3 | 335.7 | 348.3 | 367.0 |

Figure 10

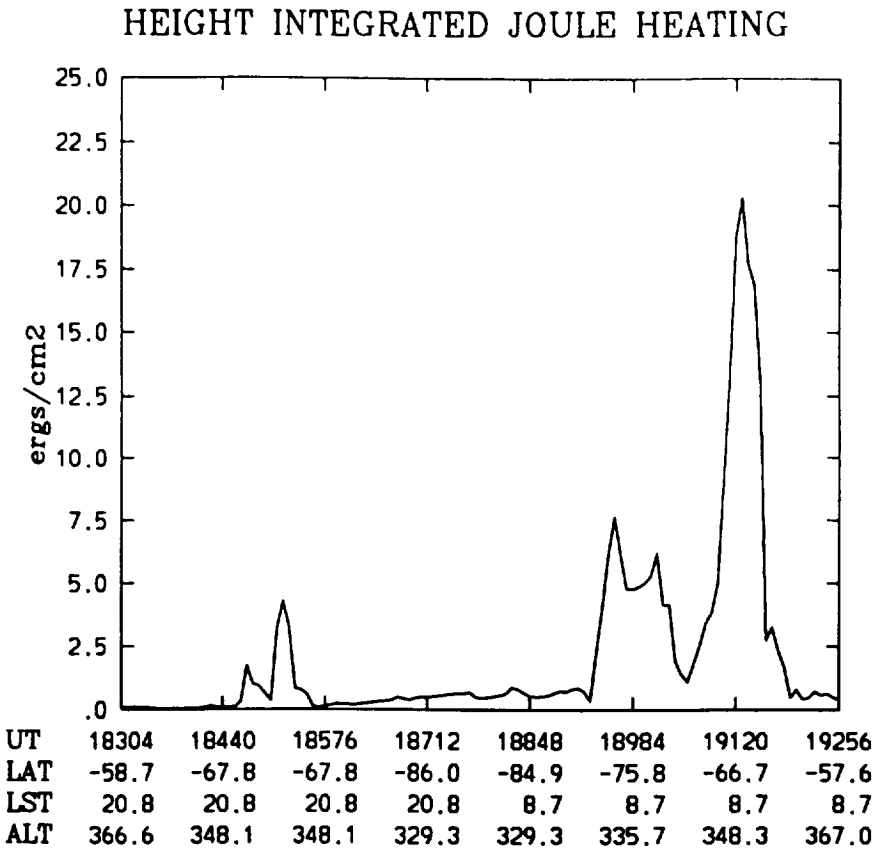


Figure 11

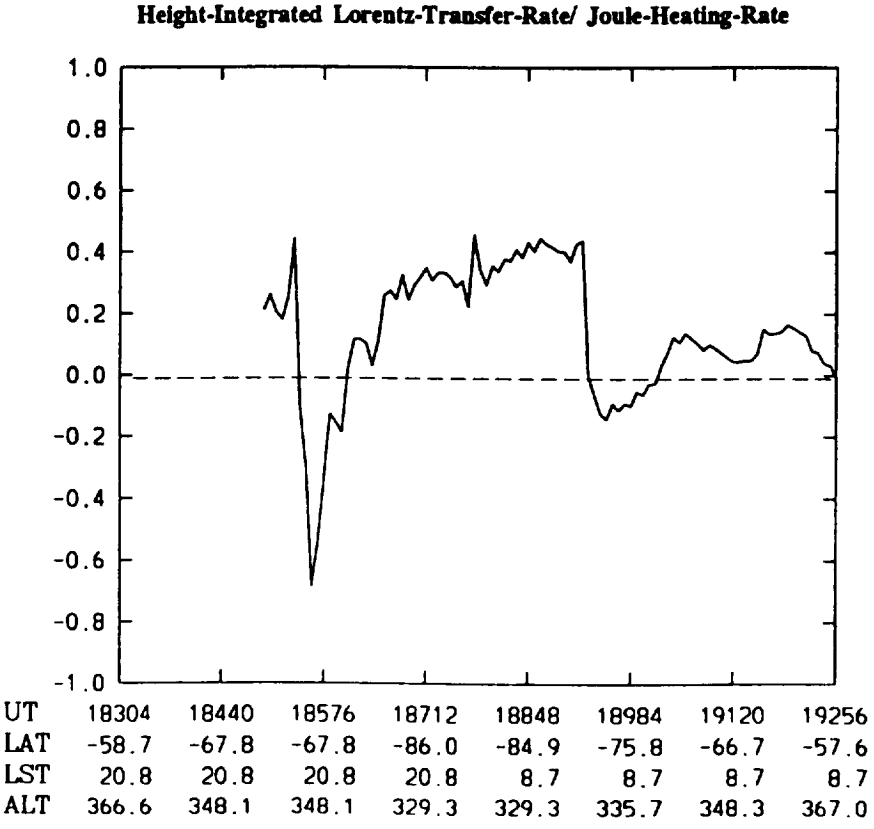


Figure 12

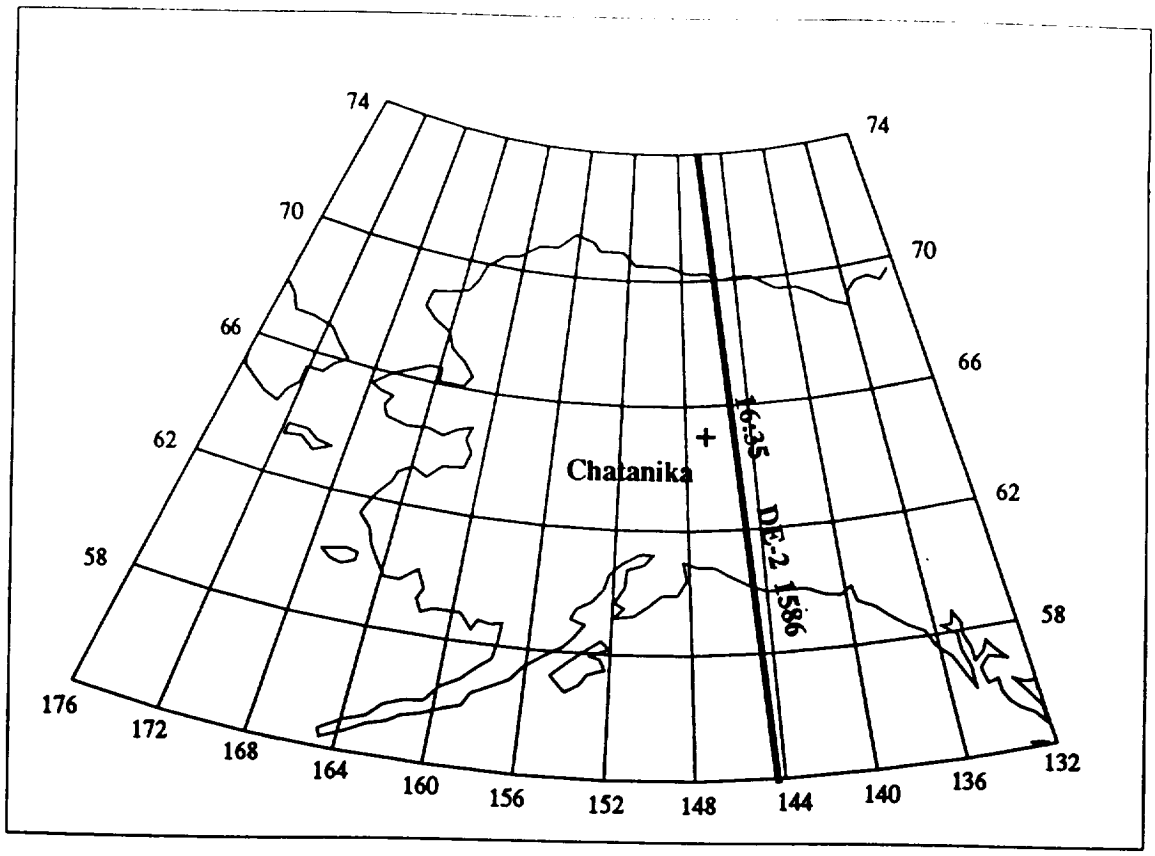
74
70
66
62
58
176
172
168
164
160
156
152
148
144
140
136
132
Chatanika
16:35 DE-2 1586

Figure 13

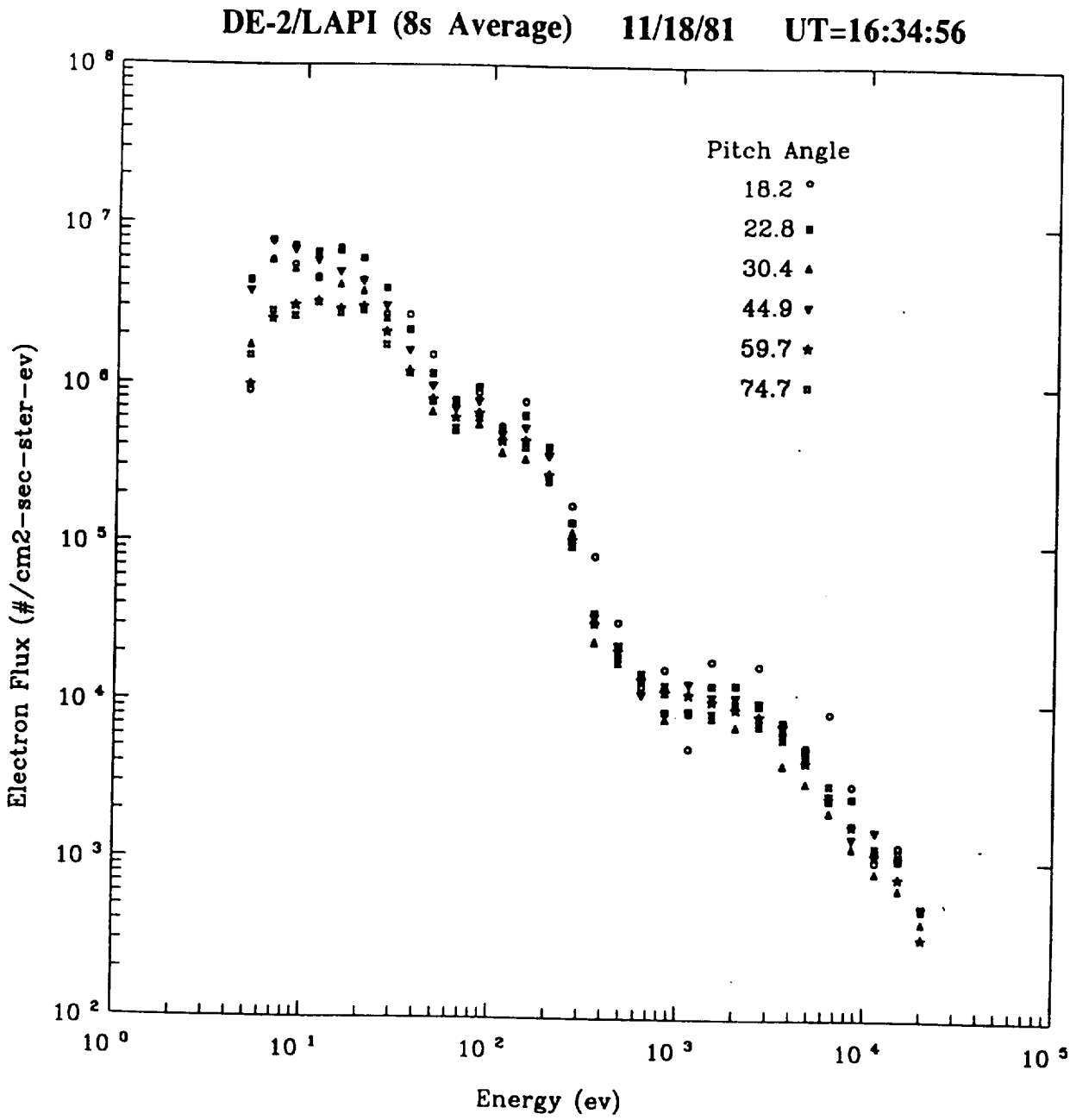
DE-2/LAPI (8s Average) 11/18/81 UT=16:34:56
Pitch Angle
18.2 °
22.8 ▪
30.4 ▲
44.9 ▼
59.7 ★
74.7 ▪
Electron Flux (#/cm2-sec-ster-ev)
Energy (ev)
10 8
10 7
10 6
10 5
10 4
10 3
10 2
10 0
10 1
10 2
10 3
10 4
10 5

Figure 14

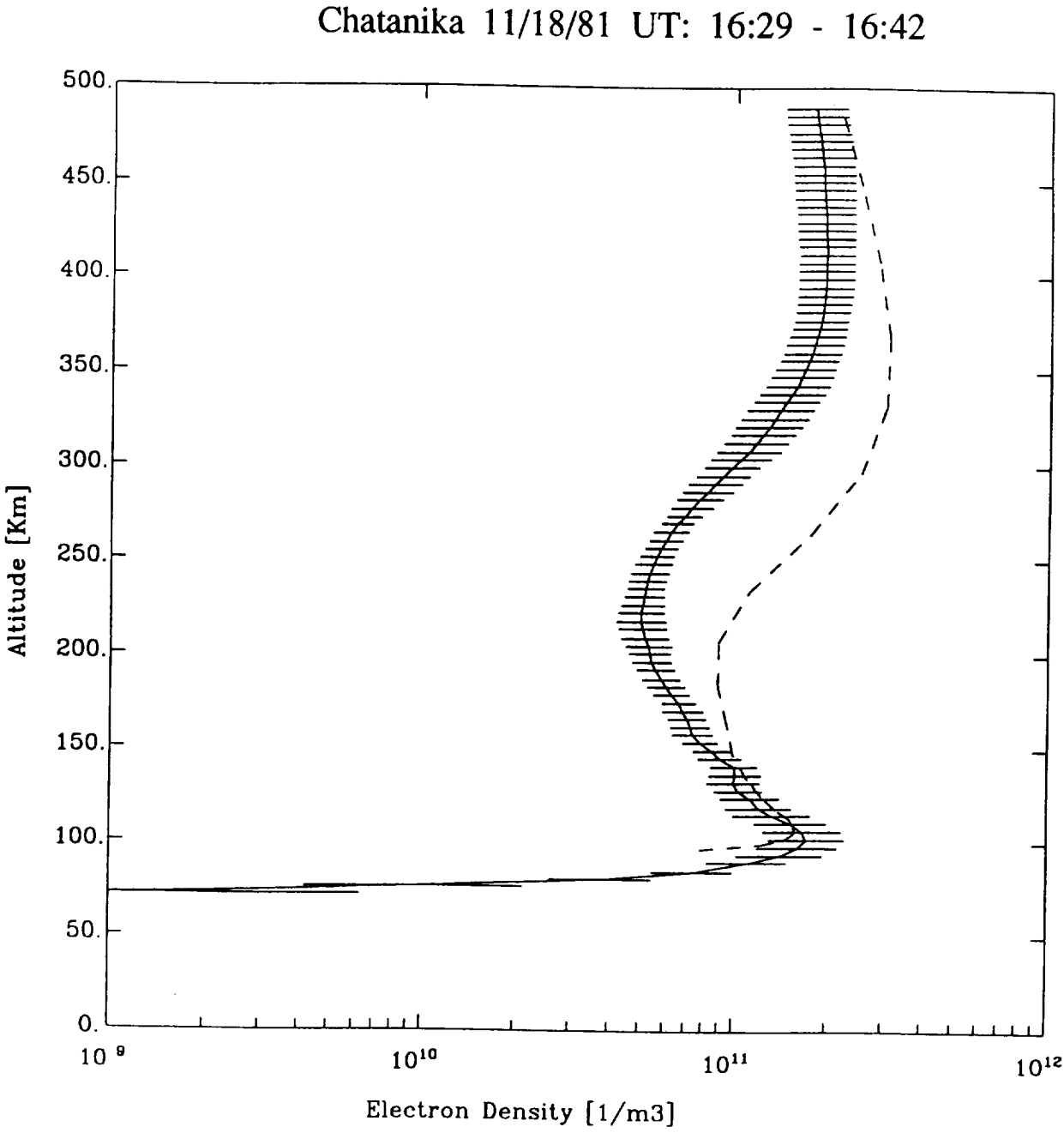
Chatanika 11/18/81 UT: 16:29 - 16:42
500.
450.
400.
350.
300.
250.
200.
150.
100.
50.
0.
Altitude [Km]
10 9
10¹⁰
10¹¹
10¹²
Electron Density [1/m3]

Figure 15

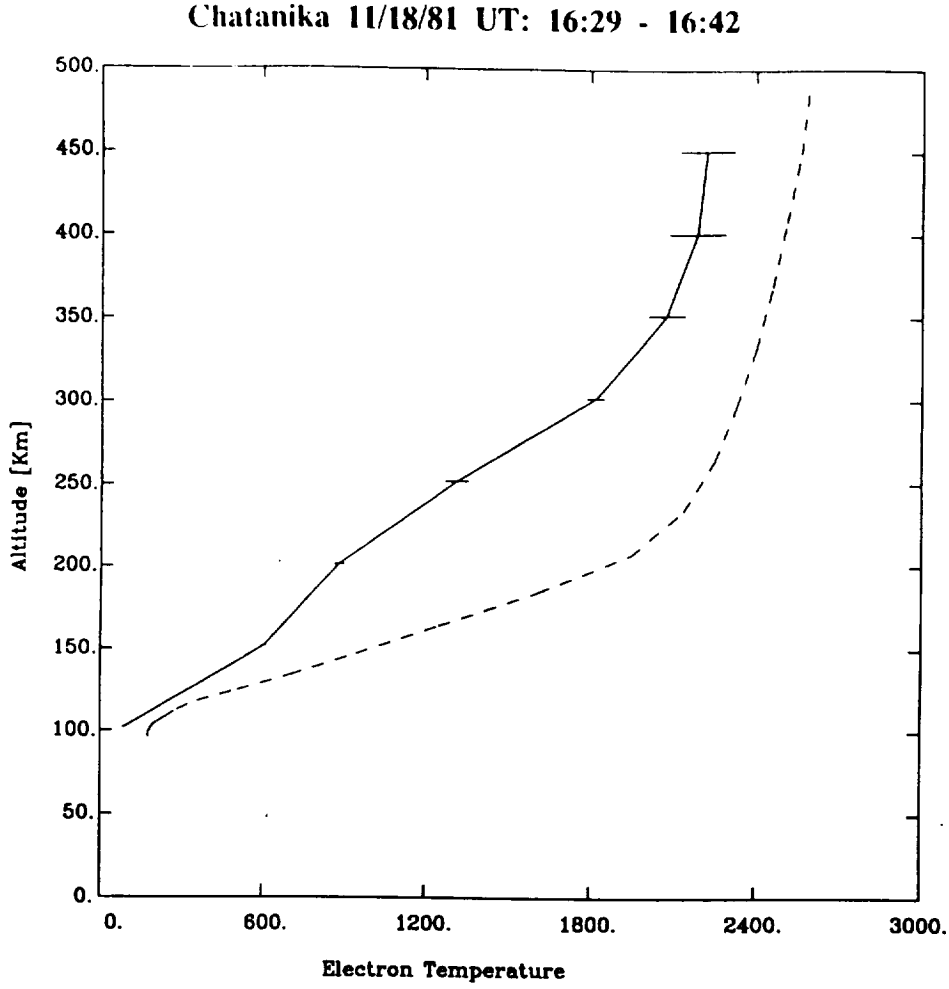


Figure 1b

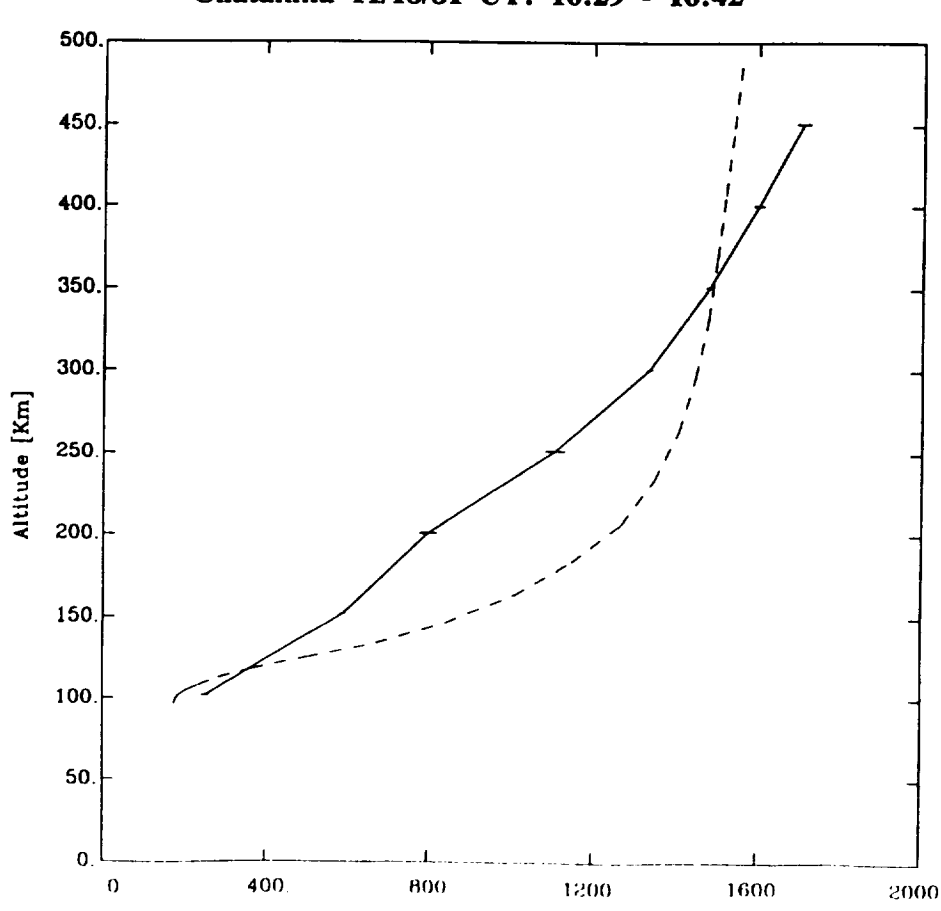


Figure 1c

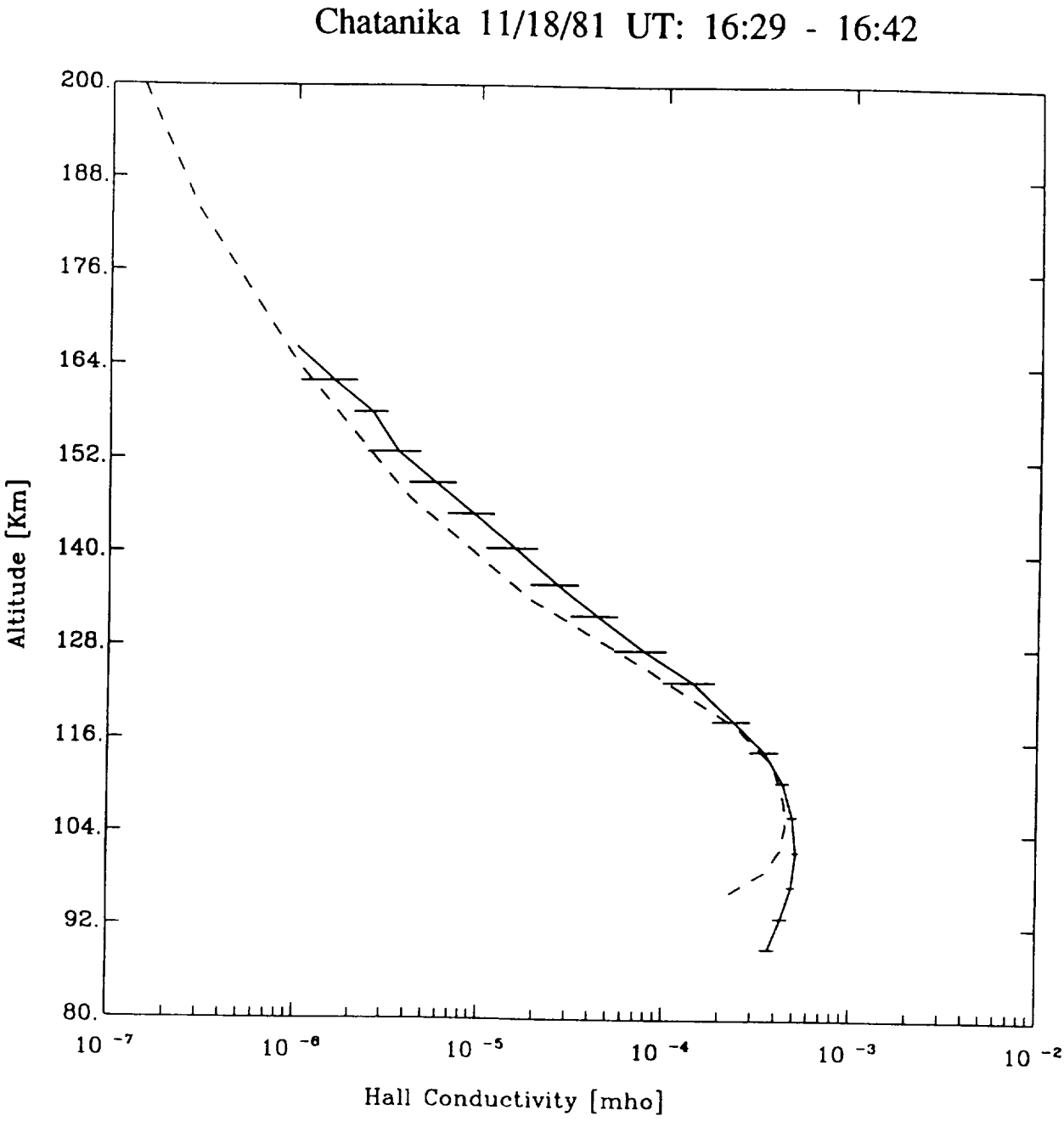
Chatanika 11/18/81 UT: 16:29 - 16:42
200.
188.
176.
164.
152.
140.
128.
116.
104.
92.
80.
Altitude [Km]
10 -7
10 -6
10 -5
10 -4
10 -3
10 -2
Hall Conductivity [mho]

Figure 18

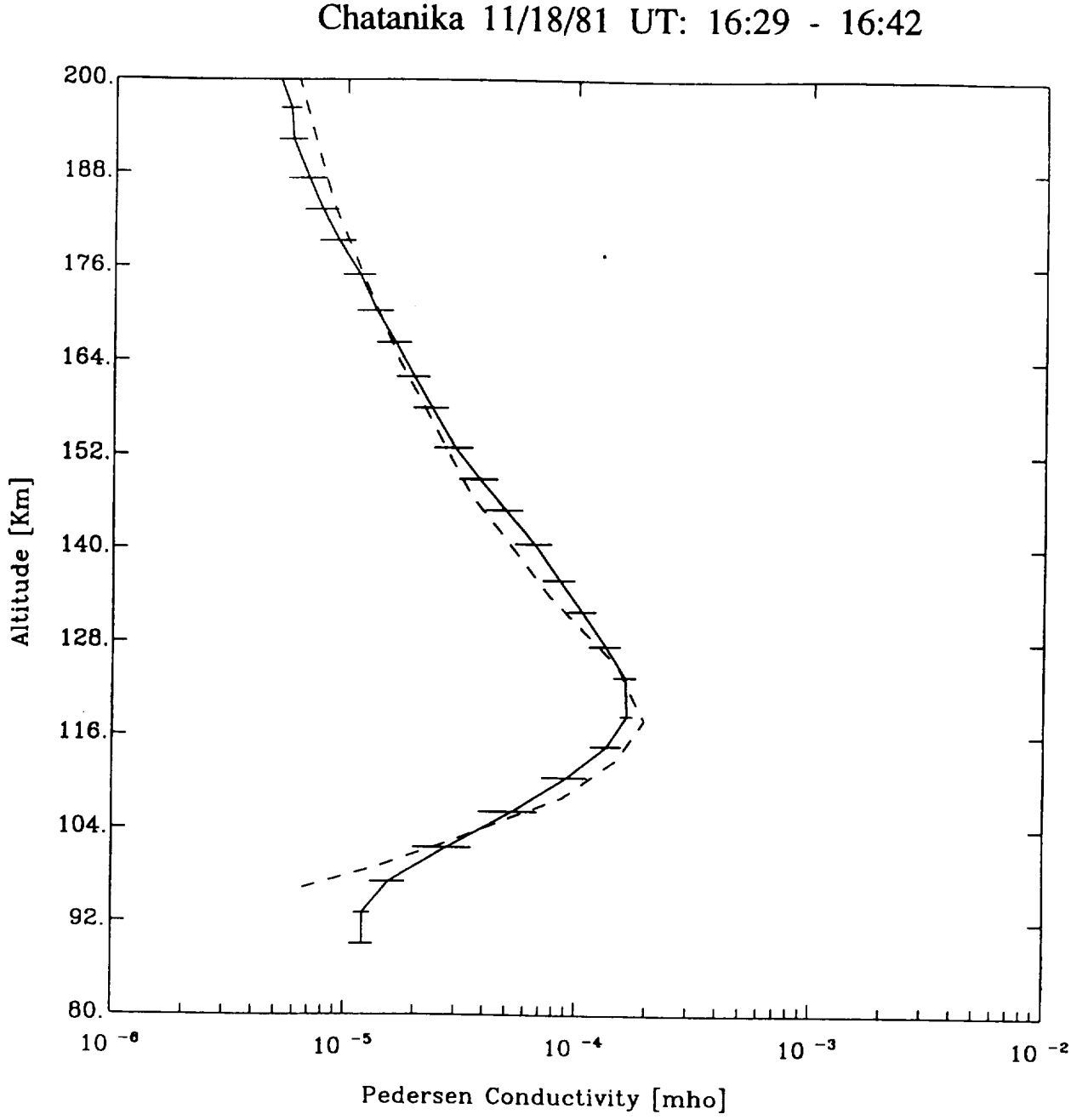
Chatanika 11/18/81 UT: 16:29 - 16:42
200.
188.
176.
164.
152.
140.
128.
116.
104.
92.
80.
Altitude [Km]
10 -6
10 -5
10 -4
10 -3
10 -2
Pedersen Conductivity [mho]

Figure 19

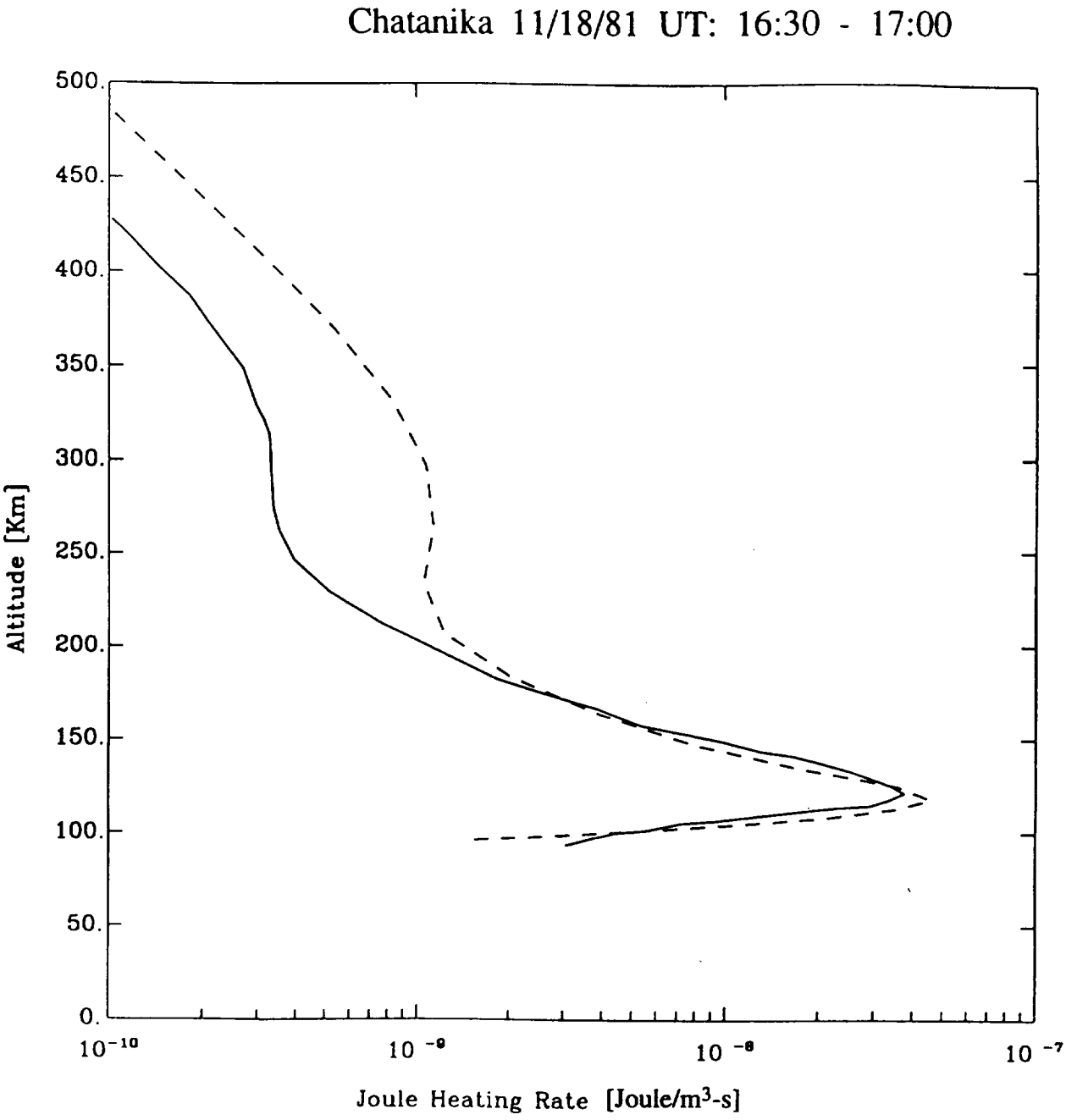
Chatanika 11/18/81 UT: 16:30 - 17:00
500.
450.
400.
350.
300.
250.
200.
150.
100.
50.
0.
Altitude [Km]
10⁻¹⁰
10⁻⁹
10⁻⁸
10⁻⁷
Joule Heating Rate [Joule/m³-s]

Figure 20